Occurrence frequency of subcritical Richardson number assessed by global high-resolution radiosonde and ERA5 reanalysis

Jia Shao[1]; Jian Zhang[2]*; Wuke Wang[3]; Shaodong Zhang[4]; Tao Yu[2]; Wenjun Dong[5,6]

[1] College of Informatics, Huazhong Agricultural University, Wuhan 430070, China

[2] Hubei Subsurface Multi-scale Imaging Key Laboratory, School of Geophysics and Geomatics, China University of Geosciences, Wuhan 430074, China

[3] School of environmental studies, China University of Geosciences, Wuhan 430074, China

[4] School of Electronic Information, Wuhan University, Wuhan 430072, China

[5] Center for Space and Atmospheric Research (CSAR), Embry-Riddle Aeronautical University, Daytona Beach, FL, USA

[6] Global Atmospheric Technologies and Sciences (GATS), Boulder, CO, USA

Correspondence to:

Dr. Jian Zhang (Email: zhangjian@cug.edu.cn)

Abstract. Kelvin Helmholtz instability (KHI) is most likely to be the primary source for clear-air turbulence that is of importance in pollution transfer and diffusion and aircraft safety. It is indicated by the critical value of the dimensionless Richardson (Ri) number, which is predicted to be 1/4 from linear stability analysis. However, Ri is fairly sensitive to the vertical resolution of the dataset; a higher resolution systematically leads to a finer structure. The study aims to evaluate the performance of ERA5 reanalysis in determining the spatial-temporal variabilities of subcritical Ri by comparing it against a near-global high-resolution radiosonde dataset during years 2017 to 2022 and further highlight global climatology and dynamical environment of subcritical Ri. Overall, the occurrence frequency of $Ri<1/4$ is inevitably underestimated by the ERA5 reanalysis over all climate zones at all heights from near-ground up to 30 km, compared to radiosonde, due largely to the severe underestimation in wind shears. Otherwise, the occurrence frequency of $Ri<1$ in ERA5 is climatologically consistent with that from $Ri<1/4$ in radiosondes in the free troposphere, especially over the midlatitude and subtropics in the Northern/Southern Hemisphere. Therefore, we argue that threshold value of Ri could be approximated as 1 rather than 1/4 when using ERA5-based Ri as proxy for KHI. The occurrence frequency of subcritical Ri revealed by both datasets exhibits significant seasonal cycles over all climate zones. In addition, it is positively correlated with the standard derivation of orography at low-levels and is exceptionally strong over the Niño 3 region at heights of 6–13 km. Furthermore, high occurrence of subcritical Ri would likely be accompanied by strong wind speeds and intensive orographic or non-orographic gravity waves.

Key words: High-resolution radiosonde; ERA5 reanalysis; Wind shears; Richardson number; Gravity waves

Introduction

Kelvin Helmholtz instability (KHI) is a common phenomenon in the atmospheric boundary layer and the free atmosphere (Muschinski and Wode, 1998), and its wavelengths and depths span a wide range of scales throughout the atmosphere, varying from few meters or less to 10s of km (Fritts et al., 2011). It contributes to vertical mixing of heat, momentum, and constituents, and it acts to limit the maximum shears, just to name a few (Fritts et al., 2011). KHI along with gravity wave (GW) breaking are the most recognized instabilities in stably stratified flows (Fritts and Rastogi, 1985). KHI arises preferentially from micro- and mesoscale wind shear intensification, with maximal occurrence frequency near synoptic scale upper-level frontal zones near jet streams, with mountain waves, and above the tops of severe thunderstorms (North et al., 2014). Large wind shear is commonly associated with regions where stability changes rapidly (e.g., near the top of the boundary layer) and the large wind gradient in jet stream (Grasmick and Geerts, 2020). In a changing climate, wind shear in the North Atlantic upper-level jet stream could be increased (Lee et al., 2019), which may increase clear-air turbulence at cruise altitudes. In turn, KHI can reduce wind shears and alter tracer gradients where turbulence and mixing are most intense (Fritts et al., 2022).

KHI influences depend on the spatial scales at which they lead to turbulence (Fritts et al., 2022). Turbulence is by far the most common cause of serious injuries to aircraft (Williams and Joshi, 2013). Convective instability, shear instability, KHI, and GW breaking are known to be the major sources for turbulence (Sharman et al., 2012; Ko et al., 2019; 2022). KHI requires a sufficiently large Reynolds number and a Richardson (Ri) number sufficiently below 1/4 to enable KHI formation and subsequent secondary instability leading to turbulence (Fritts et al., 2022). Ri is not a good guide to instability character in general, and $Ri>1/4$ does not assure flow stability for superpositions of mean and GW motions. Despite these caveats, $Ri<1/4$ does provide a reasonable guide to expected local KHI structure in cases where clear KH billows arise, according to the

85   simulation in the mesosphere and lower thermosphere region (Fritts et al., 2014). Values

86   of Ri close to zero favor strong instability, deep billows, and relatively intense

87   turbulence, whereas values of Ri closer to 1/4 favor weak instability, shallow billows

88   (Fritts et al., 2011). The Richardson number criterion can be applied as a turbulence

89   diagnostic in numerical model output (e.g. Sharman and Pearson, 2017), and it has been

90   used as such in climatological studies on the occurrence of clear air turbulence (Jaeger

91   and Sprenger, 2007). Kunkel et al. (2019) includes a brief discussion on the capability

92   of ECMWF models based on case studies to resolve subcritical Richardson numbers,

93   and argues that the threshold value of Ri (Rit) taken as 1 might be a good proxy for

94   observed KHI. A very recent study by Lee at al. (2023) also sets Rit from 0–1 in their

95   climatology on the upper troposphere and lower stratosphere turbulence diagnostics.

96   Moreover, Zhang et al. (2022) shows that over half of turbulence exists below $Ri<1$

97   when the environment is beneficial for the development of turbulence.

98   Turbulent mixing is of crucial importance to mass, energy, momentum transfer, the

99   dispersion of pollutants, and stratosphere-troposphere exchange. In numerical models,

100   turbulent dissipation rate, turbulent diffusivity and other parameters representing

101   turbulent mixing efficiency are the most basic parameters, which need to be accurately

102   parameterized to evaluate the impact of turbulence effect on matter and energy

103   distribution (Gavrilov et al., 2005). However, due to the intermittent nature of

104   turbulence it is generally not resolved in (global) numerical weather prediction models,

105   even at nowadays common/states of the art horizontal resolutions of the order of tens

106   of kilometers (Sandu et al., 2019), and it presents a challenge both in observation and

107   numerical modeling (Sharman et al., 2012; Homeyer et al., 2014; Plougonven and

108   Zhang, 2014). For this reason, the indices of turbulence, such as large wind shear, small

109   Ri and the negative squared Brunt-väisälä frequency, could be a great tool to

110   characterize turbulence (Jaeger et al., 2007).

111   The Richardson number is estimated by the finite differences across thin layers and

112   is quite sensitive to the vertical resolution of measurements (Haack et al., 2014). Thus,

113   a proper estimation of Ri requires a high-resolution measurement of temperature and

114   wind speed. The near-global distributed radiosonde site offers a unique opportunity to

investigate the climatology of subcritical Ri occurrence frequency. The overview of subcritical Ri occurrence by using a near-global high-resolution (10-m) radiosonde data was presented in Zhang et al. (2022), and a close association between subcritical Ri occurrence frequency and turbulence fraction has been found. However, the global climatology characteristic of subcritical Ri remains most unclear, especially over oceans where the radiosonde network has a poor coverage.

By comparison, ERA5 global reanalysis can provide a seamless coverage of temperature and wind, and it is the last version of the European Centre for Medium-Range Weather Forecasts (ECMWF) model and has 137 model levels (Hersbach et al., 2020). Its predecessor, ERA-Intrim, was found in particular wind shear a factor of 2–3 lower simulated based on high-resolution radiosondes (Houchi et al., 2010). Moreover, results show that whatever the location and the geophysical conditions considered, biases between ERA-Interim and balloon wind measurements increase as a function of altitude (Duruisseau et al., 2017). Recent studies have suggested that the structure and variability of the trade winds in the lower troposphere are reasonably reproduced in the ERA5 reanalysis based on the EUREC4A field campaign (Savazzi et al., 2022). However, the similar comparison between ERA5 and high-resolution radiosonde across a near-global area has largely been undetermined. The proper estimation of wind shear and Brunt-Väisälä frequency is essential for the determination of Ri.

Thus, our objectives are to: (1) Evaluate the performance of ERA5 at different heights and climate zones in estimating wind shear and small Richardson number occurrence frequencies, in comparison with a large high-resolution radiosonde dataset spanning the years from 2017 to 2022. (2) Based on the validation and comparison results, we pose a question: how to use ERA5 for subcritical Ri estimation? (3) The global climatology of subcritical Ri occurrence based on versatile measurements and model products. (4) The dynamic environment (GWs and mean flow) of subcritical Ri. These works would be valuable for the understanding of the global distribution of subcritical Ri, and furthermore, turbulence fraction. To this end, this analysis is organized as follows. Section 2 shows the data and methods used. Section 3 represents the climatological variation of subcritical Ri and its comparison with radiosonde.

145   Section 4 ends with a summary.

146

2 Data and methods

2.1 High-resolution radiosonde dataset

As described in Guo et al. (2021) and Zhang et al. (2022), a high vertical resolution radiosonde (HVRRS) dataset gained from several organizations was adopted, spanning January 2017 to October 2022, in a total of 5.8 years. The organizations include the China Meteorological Administration (CMA), the U.S National Oceanic and Atmospheric Administration (NOAA), the Global Climate Observing System (GCOS) Reference Upper-Air Network (GRUAN), the Centre for Environmental Data Analysis of the United Kingdom (CEDA), University of Wyoming, Deutscher Wetterdienst, and ECMWF. In total, around 0.95 million radiosonde profiles from 434 radiosonde stations released at regular synoptic times of 0000 UTC and 1200 UTC were collected to determine the value of Ri. These profiles were sampled at 0.5 Hz or 1 Hz, corresponding to a vertical resolution of approximately 10 m or 5 m. Thus, all the profiles were evenly interpreted to 10 m resolution in vertical by applying a cubic spline interpolation. In addition, the sounding with the burst height lower than 10 km above ground level (a.g.l.) was directly discarded for further study. Meteorological variables, including temperature and wind speed, were prepared for the Ri estimation.

One of the shortages of radiosonde measurements is its inadequate concentration over the polar and ocean regions (Xia et al., 2021). The geographical distribution of total profile number of each radiosonde station is demonstrated in Figure S1 in the supporting information. The released radiosoundings over Europe, the United States, and Australia have good geographical coverage and time duration. Over some islands of oceans (e.g., the Pacific Ocean) there are dozens of stations that can provide high-resolution measurement. Over the polar regions, there are around thirty stations.

2.2 ERA5 reanalysis and the collocation procedure

ERA5 is the latest version of ECMWF meteorological reanalysis, benefiting from a decade of developments in model physics, core dynamics, and data assimilation (Hersbach et al., 2020). The wind and temperature fields are modelled by the ERA5 reanalysis on a spatial resolution of 0.25° latitude/longitude and a temporal resolution of 1 hour. The reanalysis has 137 model levels, giving a vertical resolution of approximately 300 m in the middle and upper troposphere. The vertical resolution of ERA5 is illustrated in Figure S2. Compared to ERA5, the HVRRS does not provide global seamless observations. Thus, the collocation procedure between reanalysis and HVRRS goes as follows: (1) the matched grid of ERA5 reanalysis is the nearest neighbor of radiosonde station; (2) the regular synoptic start time of radiosonde and reanalysis needs to keep exact the same; (3) the pressure coordinate of reanalysis is converted into geometric altitude to match with HVRRS.

In addition, the standard deviations of orography (SDOR) and the gravity wave dissipation due to the effects of stress associated with unresolved valleys, hills and mountains in ERA5 reanalysis are extracted.

The relative error between HVRRS-based and ERA5-based quantities is estimated by the ratio of deviations between HVRRS and ERA5 derived quantities to the HVRRS one.

2.3 The occurrence frequency of subcritical *Ri* and its uncertainty

Based on a linear theory, the threshold *Ri* (*Rit*) defines the threshold where the air flow changes from stability to turbulence, and it is usually suggested to be 1/4 (Haack et al., 2014). *Ri* is formulated as:

$$\text{Ri} = \bar{N}^2/\bar{S}^2 \qquad (1)$$

where N is the Brunt-Väisälä frequency ($\sqrt{\frac{g}{\theta}\frac{d\theta}{dZ}}$), S is the vertical wind shear ($\sqrt{(\frac{dU}{dZ})^2 + (\frac{dV}{dZ})^2}$), and the overbar denotes a moving average in 200-m step to eliminate the influence of small-scale fluctuations, such as turbulence and small-scale waves. In

198 addition, horizontal winds measured under radiosonde at the scale of a few tens of

199 meters are affected by the chaotic movements of the gondola due to the pendulum and

200 to the balloon's own movements (Ingleby et al., 2022). For 10-m radiosondes, the

201 moving average in a step of 200-m could offset the effect of chaotic movements, at least

202 to some extent. In this case, the matching quantities that include Ri, wind shear, and the

203 Brunt-Väisälä frequency between radiosonde and ERA5 profiles are actually handled

204 in averaged 200 m intervals.

205   The Richardson number calculated from Eq.(1) depends on the vertical resolution

206 of the underlying data, as well as on the averaging interval. Ultimately, this influences

207 the estimated occurrence frequency for subcritical Richardson numbers as a proxy for

208 KHI. We resample the HVRRS data to 50 m and 100 m, and range the length scale of

209 overbar from 100 m to 500 m, to diagnose the uncertainties raised by the length scale

210 of segments and the vertical resolution of dataset. As indicated in Figure 1, under the

211 same length scale of overbar, a sparser vertical grid inevitably leads to a lower

212 occurrence frequency of subcritical Ri. For instance, as the length scale set to 100 m,

213 the occurrence frequency of Ri<1/4 at 0–2 km above sea level (a.s.l.) decreases from

214 22% when vertical resolution is equal to 10 m to 16% for a vertical resolution of 50 m.

215 Moreover, a longer length-scale of segment generally yields a smaller occurrence

216 frequency. For example, as the vertical resolution of radiosonde is equal to 10 m, the

217 occurrence frequency at 10–15 km decreases from 9% when the length scale of segment

218 equals 100 m to 1% when it equals 500 m. It is interesting to note that the occurrence

219 frequency under a vertical resolution of 50 m and a segment interval of 100 m is a bit

220 larger than that under a vertical resolution of 10 m and a segment of 200 m, possibly

221 implying the fact that a shorter segment interval could be expected for a sparser vertical

222 resolution.

223 **2.4 Gravity wave energy**

224   The GW energy is extracted based on the broad spectral method, according to Wang

225 and Geller (2003). In this method, the magnitude of measured zonal wind (u),

226 meridional wind (v), and temperature (T) consisting of background states (u_0, v_0 and

227 T_0) that are determined by applying a second-order polynomial fit (Chen et al., 2018;

228 Zhang et al., 2022) and perturbations. Therefore, total perturbations are derived as:

$$(u', v', T') = (u, v, T) - (u_0, v_0, T_0) \qquad (2)$$

230 The perturbations could include measurement noises, KH waves, GWs, and

231 planetary waves. Only the perturbations with vertical wavelengths of 0.3–6.9 km are

232 considered as GWs (Wang and Geller, 2003). The mean vertical wavelength of GWs is

233 about 2 km (Wang et al., 2005), and therefore, the lowermost threshold of 0.3 km could

234 have little influence on the GW energy. However, the retrieval of the largest wavelength

235 is not well determined, which is acknowledged as the radiosonde's "observational filter"

236 (Alexander, 1998). By applying this band-pass filter, the average gravity-wave kinetic

237 energy per unit mass (energy density) and the average potential energy density can be

238 expressed as:

$$E_k = \frac{1}{2}\left[\overline{u'^2} + \overline{v'^2}\right] \qquad (3)$$

$$E_p = \frac{1}{2}\frac{g^2\overline{\hat{T}'^2}}{N^2} \qquad (4)$$

241 where g is the gravitational constant, $\hat{T}' = T'/\bar{T}$ the normalized perturbation

242 temperature, and the overbar indicates an averaging over the tropospheric segment,

243 which is chosen as 2–8.9 km for all regions, expect the polar region, and it is selected

244 as 2–7.4 km for the polar region (Wang and Geller, 2003). Eventually, the total GW

245 energy E_t is the sum of E_k and E_p.

3 Results and Discussions

3.1 Comparisons of wind shear between HVRRS and ERA5 reanalysis

248 The variations in vertical shear of horizontal wind speed and the squared Brunt-

249 väisälä frequency entirely determine the Ri magnitude. Figure 2 provides an overview

250 of the spatial distribution of wind shear at heights of 0–2 km a.s.l. and 10–15 km a.s.l.

251 obtained from the HVRRS and ERA5 reanalysis. HVRRS-based wind shear is taken

252 from Eq.(1), with a vertical resolution of 10-m. The shear at heights of 0–2 km a.s.l.

253   estimated by ERA5 reanalysis demonstrates a strong spatial variation, and it is largely

254   dependent on underlying terrains and latitudes (Fig.2a). For example, large values can

255   most likely be observed along the coastline, which could be attributed to the prevailing

256   sea-breeze circulation. As compared to the HVRRS, these shears are slightly

257   underestimated by 5.37 m/s/km, based on all sounding measurements (Fig.2b).

258   Nevertheless, a close association between averaged ERA5-reterived shears and

259   HVRRS-determined shears can be noticed in terms of geospatial distribution, with a

260   correlation coefficient of 0.36 (Fig. 2b).

261   It is noteworthy that shear in the ERA5 reanalysis at heights of 10–15 km a.s.l. is

262   significantly underestimated compared to the HVRRS, especially at middle latitudes,

263   with a mean absolute error for all stations of about 8 m/s/km (Table 1). The

264   underestimation could partly be due to the coarse vertical resolution (around 300-m) in

265   the ERA5 reanalysis in this height interval. However, the spatial distribution of the

266   ERA5 shear still exhibits a significant positive correlation with the HVRRS shear, with

267   a correlation coefficient of 0.35 (Fig.2d).

268   Following Houchi et al. (2010), the monthly shears over seven typical climate

269   zones are separately investigated (Fig. 3), which are defined as follows: polar (70°–

270   90°), mid latitudes (40°–70°), subtropics (20°–40°), and tropics (20°S–20°N). Over the

271   polar region in the Northern/Southern Hemisphere, HVRRS-based shears are

272   exceptionally strong in the lower stratosphere compared to those in the troposphere

273   (Fig.3a, g), which could be attributed to the stratospheric polar jet. However, the similar

274   altitude variation can hardly be found in ERA5-based shears that are dramatically

275   underestimated by around 14 m/s/km in the lower stratosphere (Fig.3h, n, also seen in

276   Table 1). The results in midlatitudes reach a similar conclusion (Fig.3b, f, i, m). Over

277   subtropical regions, HVRRS-based shears are consistent strong at heights of 16–21 km

278   a.s.l., just above the subtropical jet stream (Fig.3c, e). However, in the ERA5 reanalysis,

279   the region with consistently strong shears can be noticed at approximately 16 km a.s.l.

280   (Fig.3j, l), which is about 3 km lower than that in the HVRRS. One possible reason

281   might be that the model fails to resolve the further increasing shear in the lower

282   stratosphere. In the tropics, the signature of quasi-biennial oscillation (QBO) can be

283   identified in the lower stratosphere (Fig.3d, k).

284   The comparison between HVRRS-based and ERA5-based shears at three typical

285   regimes is tabulated in Table 1. These metrics highlight that ERA5-based shears are

286   underestimated by approximately 5 m/s/km, 7.5 m/s/km, 10 m/s/km at heights of 0–2

287   km, 10–15 km, and 20–25 km a.s.l., respectively, which are roughly consistent with

288   Houchi et al. (2010).

289   By comparison, the ERA5-acquired N^2 averaged from the surface to 30 km a.s.l.

290   is reliably estimated at all heights, with a relative error of around 14%, as illustrated in

291   Figure S3. This finding indicates that the ERA5 reanalysis can properly present the

292   static stability of the background atmosphere, but it is not properly coincident with

293   radiosonde in terms of the small-scale variability of dynamical structures. Due to a lack

294   of global measurement of the fine-structure of the upper-air wind, however, the

295   accuracy of ERA5-resolved shears is hard to be globally validated.

296   **3.2 Occurrence frequency of Ri<1/4 in HVRRS and ERA5 reanalysis**

297   As a prominent example, the monthly occurrence frequency of Ri<1/4 over the

298   Corpus Christi station (27.77° N, −97.5° W) during years from January 2017 to

299   October 2022 is illustrated in Figure 4. As a result, the monthly occurrence rate of

300   Ri<1/4 in the planetary boundary layer (PBL) regime determined from HVRRS is lower

301   than the ERA5-based one, with mean values of around 10.6% and 16.9%, respectively.

302   In the lowermost 2 km, the vertical resolution of ERA5 reanalysis is less than 200 m,

303   and it is less than the moving segment interval in Eq.(1). The high occurrence frequency

304   in the PBL regime could be likely related to the negative or small N^2. Especially during

305   the daytime, PBL is well mixed due to strong turbulence induced by uprising thermals

306   (Song et al., 2018). In addition, an obvious seasonal cycle of occurrence frequencies is

307   revealed by HVRRS in the middle and upper troposphere and has a maximum in winter

308   (December–January–February) and spring (March–April–May) seasons, which is

309   consistent with the finding in Zhang et al. (2019). In the vicinity of jet streams, the

310   occurrence frequency of Ri<1/4 is generally enhanced by large wind shears. However,

the ERA5 reanalysis does not provide such a seasonal cycle pattern, and the occurrence frequency of $Ri<1/4$ is significantly underestimated by around 8% (Fig.4b), which could be attributed to the underestimation in wind shears. In the lower stratosphere, both the HVRRS and ERA5 reanalysis provide a low estimation of occurrence frequencies, with a value of around 1%.

Furthermore, on a large spatial scale the occurrence frequency of $Ri<1/4$ retrieved by ERA5 reanalysis is remarkably underestimated in the free atmosphere, as compared to the HVRRS. The annual variation of the occurrence frequency of $Ri<1/4$ over seven climate zones at 10 to 15 km a.s.l. indicated by HVRRS and ERA5 reanalysis is further demonstrated in Figure 5. It is clearly seen that the occurrence frequency of $Ri<1/4$ provided by ERA5 reanalysis is underestimated in all months, over all climate zones, possibly implying that, in the free atmosphere, the threshold value of 1/4 in Eq.(1) is too small for the ERA5 reanalysis to capture the occurrence of KHI.

However, the ERA5 reanalysis data is non-uniformly sampled in altitude. Its vertical resolution drops from about 100-m in the boundary layer to about 500-m in the lower stratosphere. In contrast, radiosondes have a vertical resolution of 10-m at all heights. Therefore, we selected four typical heights and vertically interpolated the radiosonde to the same height resolution as ERA5 for comparison. The four height intervals are 0.8–1.3 km, 2.2–3.2 km, 6–15 km and 20–21 km a.s.l., as shown in Table 2. In these height intervals, the vertical resolution of ERA5 is about 100-m, 200-m, 300-m and 400-m respectively. Even at the same vertical resolution, ERA5 still seriously underestimates the value of $OF(Ri<1/4)$ at all heights and all climate zones. These results indicate that the greatest difficulty in evaluating subcritical Ri with ERA5 is that its simulation of wind shears might be seriously underestimated compared with radiosonde. As illustrated in Table 3, even accounting for the fact that ERA5 has a comparable vertical resolution of radiosonde, wind shears in ERA5 reanalysis are still underestimated by around 51.9%, 50.7%, 44.5%, and 62.5% at 0.8–1.3 km, 2.2–3.2 km, 6–15 km and 20–21 km a.s.l., respectively. In order to obtain an occurrence frequency of subcritical Ri from ERA5 reanalysis that is comparable with radiosonde-based $OF(Ri<1/4)$, the Rit for ERA5 should be set larger than 1/4. For instance, at 0.8–1.3 km

341 and 2.2–3.2 km a.s.l., the Rit equals 1 could be a proper choice for ERA5 reanalysis,

342 rather than 1/4 (Table 2). More generally, $0.5<Rit<1.5$ could be more suitable for ERA5

343 reanalysis, compared to $Rit=1/4$.

344 Due to the huge change in the vertical resolution of ERA5, it could be difficult to

345 interpolate ERA5 into uniform data vertically with a relatively high resolution.

346 Therefore, the question posed here is, what is the proper threshold value of Ri in

347 predicting the occurrence of KHI when using the ERA5 reanalysis, compared to

348 HVRRS? The occurrence frequency of $Ri<1/4$ indicated by the HVRRS, the ERA5-

349 determined occurrence frequencies produced by $Ri<0.25$, $Ri<0.5$, $Ri<1$, $Ri<1.5$, and

350 $Ri<2$ at all heights up to 30 km a.s.l. are demonstrated in Figure 6. It is notable that over

351 all climate zones and in the free atmosphere, occurrence frequencies of $Ri<0.25$ and

352 $Ri<0.5$ obtained from the ERA5 reanalysis are underestimated, but the frequencies of

353 $Ri<1.5$ and $Ri<2$ are generally overestimated. The occurrence frequency of $Ri<1$ gives

354 a close estimation both in magnitude and spatial variation compared to HVRRS over

355 all climate zones.

356 Furthermore, the correlation coefficients between HVRRS-determined

357 occurrence frequency and the ERA5-determined frequencies indicated by different

358 threshold values of Ri at height levels of 0 to 30 km are illustrated in Figure 7. It is

359 worth noting that, in the troposphere, the ERA5-based frequencies indicated by $Ri<1$,

360 $Ri<1.5$, and $Ri<2$ are highly positively correlated with those from the HVRRS, with a

361 correlation coefficient of around 0.6 over all climate zones. In the lower stratosphere,

362 however, these coefficients rapidly decline to 0.1, which can be explained by the low

363 occurrence frequency in this height regime.

364 Combined the findings in Figures 6 and 7, in the free troposphere, we can conclude

365 that the ERA5-determined occurrence frequency of $Ri<1$ is closest to the frequency of

366 $Ri<1/4$ based on the HVRRS. In the free atmosphere, KHI is the dominant source for

367 clear-air turbulence (CAT) that is a well-known hazard to aviation. Therefore, the global

368 characterization of KHI occurrence frequency in the free atmosphere obtained from

369 ERA5 reanalysis could be of importance for understanding the spatial-temporal

370 variation of CAT. In the following sections, the occurrence frequency of subcritical Ri

371 (hereinafter $OF(Ri<Rit)$) is based on $Ri<1$ in ERA5 reanalysis and $Ri<1/4$ in HVRRS,

372 unless otherwise noted.

373 Finally, it is noteworthy that $OF(Ri<Rit)$ includes the component of $Ri<0$ that

374 indicates potential for convective instability. However, both ERA5 and HVRRS are

375 difficult to totally avoid $Ri<0$ when calculating Ri. Therefore, we evaluated the

376 proportion of $Ri<0$ in all $Ri<Rit$ in the two datasets to evaluate the possible contribution

377 from convection, as shown in Figure 8. For HVRRS, the proportion of $OF(Ri<0)$ drops

378 sharply from about 40% in the PBL region to about 18% at 5–15 km a.s.l.. Similarly,

379 for ERA5 its proportion drops from about 40% in the lowermost part of the atmosphere

380 to about 2% at 5–16 km a.s.l.. These findings indicate that, in the free atmosphere,

381 $OF(Ri<Rit)$ is mainly composed of $OF(0<Ri<Rit)$, which implies that local instabilities

382 constitute most of the dynamic instability.

383 **3.3 The $OF(Ri<Rit)$ climatology**

384 For a first hint the global distributions of $OF(Ri<Rit)$ provided by the ERA5

385 reanalysis at 0–2 km a.s.l. and 10–15 km a.s.l. are displayed in Figure 9. $OF(Ri<Rit)$ in

386 the PBL region is considerably spatially heterogeneous. Over subtropical oceans in the

387 Northern/Southern Hemisphere, the intense $OF(Ri<Rit)$ can be noticed and has a

388 magnitude of around 50% (Fig.9a). In addition, over the Sahara Desert the $OF(Ri<Rit)$

389 reaches as high as 65%. Interestingly, the spatial variation in $OF(Ri<Rit)$ ensembled by

390 years 2017 to 2022 keeps high consistency with that of planetary boundary layer height

391 (PBLH) over oceans, such as the Pacific Ocean near Japan and the Atlantic Ocean near

392 U.S., as shown in Figure S4. However, at 0–2 km a.s.l., the spatial variation of

393 $OF(0<Ri<Rit)$ exhibits a large difference with that of $OF(Ri<Rit)$ in terms of magnitude,

394 as shown in Figure S5. It is around 40% (20%) lower than that of $OF(Ri<Rit)$ over

395 subtropical oceans (Australia and North Africa). At heights of 10–15 km a.s.l., intensive

396 $OF(0<Ri<Rit)$ can be viewed over subtropic regions and has a value of around 10%

397 (Fig.9b), which is likely attributed to upper tropospheric jets.

398 In comparison, the spatial-temporal variability of $OF(Ri<Rit)$ indicated by HVRRS

keeps highly consistency with that of ERA5 reanalysis over all climate zones and in the free troposphere, except in the stratosphere of polar region (Figure 10). Seasonal cycles can be detected by both the HVRRS and ERA5 reanalysis over all climate zones, especially over subtropics and midlatitude regions. However, the ERA5-based $OF(Ri<Rit)$ can only reflect the large scale structure of the cycles, and it is hard to quantify the detailed variation like the HVRRS does.

Furthermore, the seasonal variation of $OF(Ri<Rit)$ with $Rit=1/4$ for HVRRS and $Rit=1$ for ERA5 for all climate zones is further analyzed in Figure 11. In the midlatitudes and subtropics, the $OF(Ri<Rit)$ exhibits maximum values in the PBL, as well as a local minimum in the middle troposphere and a local maximum at altitudes around 9 km. In the stratosphere the occurrence frequencies decrease to values of the order of 1% (Fig.11b,c,e,f). Over tropic regions, a primary peak can be clearly noticed at around 13 km, with a maximum of 12% for the HVRRS and 20% for the ERA5 reanalysis (Fig.11d, k). The seasonality over the tropical region could be related to some large scale flow features like the Summer Asian Monsoon and the tropical easterly jet (Roja Raman et al., 2009; Sunilkumar et al., 2015; Kaluza et al., 2021). Over polar regions, the tropospheric $OF(Ri<Rit)$ is significantly lower than that over other climate zones, with values ranging from around 4% at heights of 2–8 km to 1% in the lower stratosphere (Fig.11a,g).

In Table 4, the mean $OF(Ri<Rit)$ magnitudes over seven climate zones and at three typical altitude regimes are listed. At 0–2 km a.s.l., the ERA5-based $OF(Ri<Rit)$ is about 20% larger than that of the HVRRS-based one. At 10–15 km a.s.l., the ERA5-based $OF(Ri<Rit)$ is reasonably well estimated, except that it is overestimated by around 5.8% over the tropics region. In addition, ERA5 underestimates $OF(Ri<Rit)$ by around 0.5% in the lower stratosphere.

According to Fig.9a, it seems that low-level continental $OF(Ri<Rit)$ is dependent on underlying terrains. However, the vertical resolution of ERA5 in the PBL decreases sharply, leading to the fact that the resolution of the PBL data over the region with high elevations can be significantly lower than that of regions with low elevations, which could bring great challenges to the analysis of the impact of topography on low-level

429   *OF*(*Ri<Rit*). Therefore, we investigate the association of low-level HVRRS-determined

430   *OF*(*Ri<Rit*) with the standard deviation of orography (SDOR). At heights of 1–2 km

431   a.g.l., the underlying terrain with a large SDOR generally corresponds to a high

432   *OF*(*Ri<Rit*), with a correlation coefficient between *OF*(*Ri<Rit*) and SDOR of 0.24.

433   Then, the coefficient decreases to 0.15 at 3–4 km a.g.l. (Fig.12b), and eventually, it

434   equals 0.14 at 5–6 km a.g.l. (Fig.12c). These findings indicate that, complex terrain

435   may locally enhance *OF*(*Ri<Rit*).

436   Moreover, it is quite evident from Fig.9b and Fig.S5 that both *OF*(*Ri<Rit*) and

437   *OF*(0<*Ri<Rit*) are largely enhanced over the tropical ocean associated with the El Niño

438   Southern Oscillation (ENSO). The most of the enhanced *OF*(*Ri<Rit*) can be identified

439   over the Niño 3 region (5° N–5° S, 150° W–90° W), and the time-height cross section

440   of *OF*(*Ri<Rit*) during years of 2000 to 2022 is illustrated in Figure 13. The *OF*(*Ri<Rit*)

441   at height region of 6–13 km are evidently large, with values of around 40%, which is

442   about 20% larger than the climatological mean value (Fig.10j). More specifically,

443   *OF*(*Ri<Rit*) during time periods of La Niña events is obviously stronger than that during

444   the EI Niño periods. The identification of ENSO events is based on Ren et al. (2018),

445   Li et al. (2022), and Lv et al. (2022). It is also worth recalling here that the wind shear

446   does not exhibit such an anomaly over the Niño 3 region (Fig.2c), implying that the

447   *OF*(*Ri<Rit*) anomaly could likely be attributed to the ENSO-related tropical convective

448   heating in the upper troposphere, leading to a low Brunt-Väisälä frequency.

449   **3.4 The dynamical environment of *OF*(*Ri<Rit*) in the free troposphere**

450   In the free troposphere where the convection activity is generally weak, KHI is

451   preferentially generated from strong wind shear, which may be closely associated with

452   mean flows and wave activities.

453   The propagation of GW could raise strong wind shear, and therefore generate KHI.

454   Thereby, we investigate the joint distribution of *OF*(*Ri<Rit*) with tropospheric GW total

455   energy and wind shear (Figure 14). The latitudinal variation of GW total energy exhibits

456   a double-peak structure, with two peaks at around 30° in the Northern/Southern

457   Hemisphere (Fig.14a). The joint distribution of $OF(Ri<Rit)$ with GW energy and wind

458   shear indicates that large $OF(Ri<Rit)$ (for instance, larger than 10%) generally

459   corresponds to GW energy larger than 10 J/kg or wind shear exceeds 14 m/s/km (Fig.

460   14b). Also, $OF(0<Ri<Rit)$ exhibits a similar distribution (Figure S6). Overall,

461   $OF(Ri<Rit)$ obviously increases with GW total energy (Figure S9a), possibly implying

462   that the propagation of GWs could enhance wind shear and therefore, the burst of KHI.

463   In addition, the interaction between low-level wind and mountain barrier could be

464   a source of orographic GWs (Zhang et al., 2022). We take orographic GW dissipation

465   in ERA5 reanalysis, which is the accumulated conversion of kinetic energy in the mean

466   flow into heat over the whole atmospheric column, as an indicator of the strength of

467   orographic GWs. It is interesting to note that monthly averaged orographic GW

468   dissipation and monthly ERA5-determined $OF(Ri<Rit)$ at heights from ground up to 30

469   km demonstrates a close association (Figure S7). For instance, in the middle

470   troposphere, they are positively associated over mountainous areas such as the Rocky

471   Mountains and the Alps Mountain, with correlation coefficients of around 0.5. These

472   findings also suggest that during months with strong unresolved gravity wave activity,

473   which then modify the flow and stability parameters of the resolved flow, and result in

474   an enhanced $OF(Ri<Rit)$.

475   At jet heights (10–15 km a.g.l.), a large shear can be easily induced by strong wind

476   speed. Figure 15 demonstrates the joint distribution of $OF(Ri<Rit)$ with wind speed and

477   wind shear. Similarly, large $OF(Ri<Rit)$ (> 10%) can be easily found when the wind

478   speed exceeds 25 m/s. In addition, $OF(0<Ri<Rit)$ can draw a similar conclusion (Figure

479   S8). In the middle and upper troposphere, $OF(Ri<Rit)$ almost linearly increases with

480   wind speed (Figure S9b).

481   In a short conclusion, in the free troposphere, the occurrence of KHI would favor

482   the dynamical environment with strong orographic or non-orographic GW activities

483   and relatively large mean flow (around 25 m/s).

4 Conclusion and remarks

The occurrence of KHI is potential crucial for many implications, such as aircraft safety and mass transfer, but it is very hard to be globally understood due to its fine structure. The subcritical Richardson number is commonly used as an indictor for KHI. This study uses the ERA5 as the latest reanalysis product from the ECMWF as well as a comprehensive data set of HVRRS radiosonde soundings to globally characterize the distribution of low Richardson numbers as a proxy for the occurrence of KHI, for the years 2017 to 2022.

Vertical wind shears are considerably underestimated at almost all heights and over all climate zones by the ERA5 reanalysis, compared to the HVRRS. It is noteworthy that vertical wind shear in the ERA5 reanalysis at heights of 10–15 km a.s.l. is dramatically underestimated by around 8 m/s/km, especially at middle latitudes. However, the spatial distribution of the ERA5 shear exhibits a statistically significant positive correlation with the HVRRS shear. As a result, the ERA5-determined occurrence frequency of $Ri<1/4$ is significantly underestimated. In addition, it is weak correlated with HVRRS-determined ones at most heights and over most climate zones.

However, the vertical resolution of ERA5 reanalysis sharply decreases with altitude, which is not comparable with HVRRS. Thus, to match with ERA5 reanalysis at specified height intervals, the HVRRS was vertically interpolated with resolutions spanning from 100-m to 400-m. Even at a comparable resolution, vertical wind shear is underestimated by around 50%, leading to a considerable underestimation in $OF(Ri<1/4)$, compared to radiosondes.

Interestingly, the ERA5-determined occurrence frequency of $Ri<1$ is generally consistent with the frequency of $Ri<1/4$ obtained from HVRRS, in terms of magnitude and temporal variation. Rather than $Ri<1/4$, we argue that the threshold value of $Ri<1$ could be more proper when using ERA5 reanalysis for KHI study, especially in the middle and upper troposphere over midlatitude and subtropic regions in the Northern/Southern Hemisphere, where a high consistency between HVRRS and ERA5

has been found in terms of $OF(Ri<Rit)$ magnitude. In other words, under a similar occurrence frequency, the identification of vertical segments with $Ri<1$ in ERA5 is equitable with identification of vertical segments with $Ri<1/4$ using HVRRS.

The climatology of $OF(Ri<Rit)$ exhibits significant seasonal cycles over all latitudes. A poleward decrease can be clearly identified in the middle and upper troposphere. In addition, over mountainous area, complex terrain may locally enhance low-level $OF(Ri<Rit)$. Moreover, it is immediately obvious that the both $OF(Ri<Rit)$ and $OF(0<Ri<Rit)$ in the middle and upper troposphere of the Niño 3 region is largely enhanced probably by the tropical convective heating.

Moreover, both $OF(Ri<Rit)$ and $OF(0<Ri<Rit)$ exhibit close relationship with GW activities and background mean flow. For instance, large $OF(Ri<Rit)$ (>10%) favors GW energy larger than 10 J/kg or mean flow stronger than 25 m/s. Over complex terrains, the orographic GW breaking could locally enhance $OF(Ri<Rit)$.

Those findings are valuable for pointing out the performance of the ERA5 reanalysis in terms of resolving low Richardson numbers as a proxy for KHI, in comparison with a near-global high-resolution radiosonde measurement. In addition, the spatial-temporal variability of $OF(Ri<Rit)$ over different climate zones from near-ground up to 30 km is quantitatively characterized by ERA5 and HVRRS, which could provide new insights that increase our understanding of the fine structure of upper air.

Acknowledgement

Financial support

Competing interests

The contact author has declared that neither they nor their co-authors have any competing interests

Data availability

The dataset can be accessed at ECMWF (2022).

Author contributions

JZ conceptualized this study. JS carried out the analysis with comments from other co-authors. JZ wrote the original manuscript. WW, SZ, TY, WD provided useful suggestions for the study. All authors contributed to the improvement of paper.

References

Alexander, M. J.: Interpretations of observed climatological patterns in stratospheric gravity wave variance, J. Geophys. Res. Atmos., 103(D8), 8627–8640,

20

https://doi.org/10.1029/97JD03325, 1998.

Duruisseau, F., N., Huret, A., Andral, and Camy-Peyret, C.: Assessment of the ERA-Interim winds using high-altitude stratospheric balloons, J. Atmos. Sci., 74(6), 2065–2080, https://doi.org/10.1175/JAS-D-16-0137.1, 2017.

ECMWF: ECMWF Reanalysis v5 (ERA5), European Centre for Medium-Range Weather Forecasts [data set], https://www.ecmwf.int/en/forecasts/dataset/ecmwf-reanalysis-v5, last access: 07 December 2022.

Fritts, D. C., K. Wan, J. Werne, T. Lund, and Hecht, J. H.: Modeling the implications of Kelvin-Helmholtz instability dynamics for airglow observations, J. Geophys. Res. Atmos., 119, 8858–8871, https://doi.org/10.1002/2014JD021737, 2014.

Fritts, D. C., P. M. Franke, K. Wan, T. Lund, and Werne, J.: Computation of clear-air radar backscatter from numerical simulations of turbulence: 2. Backscatter moments throughout the lifecycle of a Kelvin Helmholtz instability, J. Geophys. Res., 116, D11105, https://doi.org/10.1029/2010JD014618, 2011.

Fritts, D. C., and Rastogi, P. K.: Convective and dynamical instabilities due to gravity wave motions in the lower and middle atmosphere: Theory and observations. Radio Sci., 20, 1247–1277, https://doi.org/10.1029/RS020i006p01247, 1985.

Fritts, D. C., L., Wang, T. S., Lund, S. A., Thorpe, C. B., Kjellstrand, B., Kaifler, and Kaifler, N.: Multi-Scale Kelvin-Helmholtz instability dynamics observed by PMC Turbo on 12 July 2018: 2. DNS modeling of KHI dynamics and PMC responses., J. Geophys. Res. Atmos., 127, e2021JD035834. https://doi.org/10.1029/2021JD035834, 2022.

Grasmick, C., and Geerts, B.: Detailed dual-Doppler structure of Kelvin–Helmholtz waves from an airborne profiling radar over complex terrain. Part I: Dynamic structure, J. Atmos. Sci., 77(5), 1761–1782., https://doi.org/10.1175/JAS-D-19-0108.1, 2020.

Gavrilov, N. M., Luce, H., Crochet, M., Dalaudier, F., and Fukao, S.: Turbulence parameter estimations from high-resolution balloon temperature measurements of the MUTSI-2000 campaign, Ann. Geophys., 23, 2401–2413,

591　　　　doi:10.5194/angeo-23-2401-2005, 2005

592　Guo, J., Zhang, J., Yang, K., Liao, H., Zhang, S., Huang, K., Lv, Y., Shao, J., Yu, T.,

593　　　　Tong, B., Li, J., Su, T., Yim, S. H. L., Stoffelen, A., Zhai, P., and Xu, X.:

594　　　　Investigation of near-global daytime boundary layer height using high-

595　　　　resolution radiosondes: first results and comparison with ERA5, MERRA-2,

596　　　　JRA-55, and NCEP-2 reanalyses, Atmos. Chem. Phys., 21, 17079–17097,

597　　　　https://doi.org/10.5194/acp-21-17079-2021, 2021.

598　Haack, A., M. Gerding, and Lübken, F.-J.: Characteristics of stratospheric turbulent

599　　　　layers measured by LITOS and their relation to the Richardson number, J.

600　　　　Geophys.　　　　Res.　　　　Atmos.,　　　　119,　　　　10605–10618,

601　　　　https://doi.org/10.1002/2013JD021008, 2014.

602　Hersbach, H., Bell, B., Berrisford, P., Hirahara, S., Horányi, A., Muñoz-Sabater, J.,

603　　　　Nicolas, J., Peubey, C., Radu, R., Schepers, D., Simmons, A., Soci, C., Abdalla,

604　　　　S., Abellan, X., Balsamo, G., Bechtold, P., Biavati, G., Bidlot, J., Bonavita, M.,

605　　　　De Chiara, G., Dahlgren, P., Dee, D., Diamantakis, M., Dragani, R., Flemming,

606　　　　J., Forbes, R., Fuentes, M., Geer, A., Haimberger, L., Healy, S., Hogan, R. J.,

607　　　　Hólm, E., Janisková, M., Keeley, S., Laloyaux, P., Lopez, P., Lupu, C., Radnoti,

608　　　　G., de Rosnay, P., Rozum, I., Vamborg, F., Villaume, S., and Thépaut, J.-N.: The

609　　　　ERA5 global reanalysis, Q. J. Roy. Meteorol. Soc., 146, 1999–2049,

610　　　　https://doi.org/10.1002/qj.3803, 2020.

611　Homeyer, C. R., L. L. Pan, and Barth, M. C.: Transport from convective overshooting

612　　　　of the extratropical tropopause and the role of large-scale lower stratospheric

613　　　　stability, J. Geophys. Res. Atmos., 119(5), 2220–2240,

614　　　　https://doi.org/10.1002/2013JD020931, 2014.

615　Houchi, K., Stoffelen, A., Marseille, G. J., and De Kloe, J.: Comparison of wind and

616　　　　wind shear climatologies derived from high-resolution radiosondes and the

617　　　　ECMWF model, J. Geophys. Res.-Atmos., 115, D22123,

618　　　　https://doi.org/10.1029/2009JD013196, 2010.

619　Ingleby, B., Motl, M., Marlton, G., Edwards, D., Sommer, M., von Rohden, C., Vömel,

620　　　　H., and Jauhiainen, H.: On the quality of RS41 radiosonde descent data, Atmos.

Meas. Tech., 15, 165–183, https://doi.org/10.5194/amt-15-165-2022, 2022.

Lee, S. H., Williams, P. D., and Frame, T. H.: Increased shear in the North Atlantic upper-level jet stream over the past four decades, Nature, 572, 639–642, https://doi.org/10.1038/s41586-019-1465-z, 2019.

Lee, J. H., Kim, J.-H., Sharman, R. D., Kim, J., & Son, S.-W. Climatology of Clear-Air Turbulence in upper troposphere and lower stratosphere in the Northern Hemisphere using ERA5 reanalysis data. Journal of Geophysical Research: Atmospheres, 128, e2022JD037679. https://doi.org/10.1029/2022JD037679, 2023.

Li, X., Hu, Z. Z., Tseng, Y. H., Liu, Y., and Liang, P.: A historical perspective of the La Niña event in 2020/2021, J. Geophys. Res.-Atmos., 127(7), e2021JD035546, https://doi.org/10.1029/2021JD035546, 2022.

Lv, A., Fan, L., and Zhang, W.: Impact of ENSO Events on Droughts in China, Atmosphere, 13(11), 1764, https://doi.org/10.3390/atmos13111764, 2022.

Jaeger, E. B., and Sprenger, M.: A Northern Hemispheric climatology of indices for clear air turbulence in the tropopause region derived from ERA40 reanalysis data, J. Geophys. Res., 112, D20106, doi:10.1029/2006JD008189, 2007.

Kaluza, T., Kunkel, D., and Hoor, P.: On the occurrence of strong vertical wind shear in the tropopause region: a 10-year ERA5 northern hemispheric study, Weather Clim. Dynam., 2, 631–651, https://doi.org/10.5194/wcd-2-631-2021, 2021.

Kunkel, D., Hoor, P., Kaluza, T., Ungermann, J., Kluschat, B., Giez, A., Lachnitt, H.-C., Kaufmann, M., and Riese, M.: Evidence of small-scale quasi-isentropic mixing in ridges of extratropical baroclinic waves, Atmos. Chem. Phys., 19, 12607–12630, https://doi.org/10.5194/acp-19-12607-2019, 2019.

Ko, H. C., H. Y., Chun, R., Wilson, and Geller, M. A.: Characteristics of atmospheric turbulence retrieved from high vertical-resolution radiosonde data in the United States, J. Geophys. Res. Atmos., 124.https://doi.org/10.1029/2019JD030287, 2019.

Ko, H. C. and Chun, H. Y.: Potential sources of atmospheric turbulence estimated using the Thorpe method and operational radiosonde data in the United States. Atmos.

Res., 265, 105891, https://doi.org/10.1016/j.atmosres.2021.105891, 2022.

Muschinski, A., and Wode, C.: First in situ evidence for coexisting submeter temperature and humidity sheets in the lower free troposphere, J. Atmos. Sci., 55(18), 2893–2906, https://doi.org/10.1175/1520-0469(1998)055<2893:FISEFC>2.0.CO;2, 1998.

North, G. R., Pyle, J. A., and Zhang, F.: Encyclopedia of atmospheric sciences, Academic Press, Cambridge, Massachusetts, United States, 224 pp., 2014

Plougonven, R., and Zhang, F.: Internal gravity waves from atmospheric jets and fronts, Rev. Geophys., *52*, 33–76, https://doi.org/10.1002/2012RG000419, 2014.

Ren, H. L., B., Lu, J., Wan, B., Tian, and Zhang, P.: Identification standard for ENSO events and its application to climate monitoring and prediction in China, J. Meteorol. Res., 32, 923–936, https://doi.org/10.1007/s13351-018-8078-6, 2018.

Roja Raman, M., Jagannadha Rao, V. V., Venkat Ratnam, M., Rajeevan, M., Rao, S. V., Narayana Rao, D., and Prabhakara Rao, N.: Characteristics of the Tropical Easterly Jet: Long-term trends and their features during active and break monsoon phases, J. Geophys. Res.-Atmos., 114, 1–14, https://doi.org/10.1029/2009JD012065, 2009.

Sandu, I., A., A., van Niekerk, T. G., Shepherd, S. B., Vosper, A., Zadra, J., Bacmeister, et al: Impacts of orography on large-scale atmospheric circulation. npj Clim Atmos Sci, 2(1), 1–8, https://doi.org/10.1038/s41612-019-0065-9, 2019.

Savazzi, A. C. M., Nuijens, L., Sandu, I., George, G., and Bechtold, P.: The representation of the trade winds in ECMWF forecasts and reanalyses during EUREC^{4}A, Atmos. Chem. Phys., 22, 13049–13066, https://doi.org/10.5194/acp-22-13049-2022, 2022.

Sharman, R. D., S. B. Trier, T. P. Lane, and Doyle., J. D.: Sources and dynamics of turbulence in the upper troposphere and lower stratosphere: A review, Geophys. Res. Lett., 39, L12803, https://doi.org/10.1029/2012GL051996, 2012.

Sharman, R. D., and Pearson, J. M: Prediction of energy dissipation rates for aviation turbulence. Part I: Forecasting nonconvective turbulence. J. Appl. Meteorol. Climatol, 56(2), 317–337, https://doi.org/10.1175/JAMC-D-16-0205.1, 2017.

681 Song, J., Z.-H., Wang, and Wang, C.: The regional impact of urban heat mitigation
682   strategies on planetary boundary layer dynamics over a semiarid city, J.
683   Geophys. Res. Atmos., 123(12), 6410–6422,
684   https://doi.org/10.1029/2018JD028302, 2018.

685 Sunilkumar, S. V., Muhsin, M., Parameswaran, K., Venkat Ratnam, M., Ramkumar,
686   G., Rajeev, K., Krishna Murthy, B. V., Sambhu Namboodiri, K. V.,
687   Subrahmanyam, K. V., Kishore Kumar, K., and Shankar Das, S.: Characteristics
688   of turbulence in the troposphere and lower stratosphere over the Indian
689   Peninsula, J. Atmos. Sol.-Terr. Phys., 133, 36–53,
690   https://doi.org/10.1016/j.jastp.2015.07.015, 2015.

691 Wang, L., and Geller, M. A.: Morphology of gravity-wave energy as observed from 4
692   years (1998–2001) of high vertical resolution U.S. radiosonde data, J. Geophys.
693   Res. Atmos., 108(D16), 4489, https://doi.org/10.1029/2002JD002786, 2003.

694 Wang, L., Geller, M. A., and Alexander, M. J.: Spatial and Temporal Variations of
695   Gravity Wave Parameters, Part I: Intrinsic Frequency, Wavelength, and Vertical
696   Propagation Direction, J. Atmos. Sci., 62, 125–142,
697   https://doi.org/10.1175/JAS-3364.1, 2005

698 Williams, P. D., and Joshi, M. M.: Intensification of winter transatlantic aviation
699   turbulence in response to climate change. Nat. Clim. Chang., 3(7), 644–648,
700   https://doi.org/10.1038/nclimate1866, 2013.

701 Xia, P., Y., Shan, S., Ye, and Jiang, W.: Identification of Tropopause Height with
702   Atmospheric Refractivity, J. Atmos. Sci., 78(1), 3–16
703   https://doi.org/10.1175/JAS-D-20-0009.1, 2021.

704 Zhang, J., S. D., Zhang, C. M., Huang, K. M., Huang, Y., Gong, Q., Gan, and Zhang,
705   Y. H.: Latitudinal and topographical variabilities of free atmospheric turbulence
706   from high-resolution radiosonde data sets, J. Geophys. Res. Atmos., 124, 4283–
707   4298. https://doi.org/10.1029/2018JD029982, 2019.

708 Zhang, J., J., Guo, H., Xue, S., Zhang, K., Huang, W. Dong, et al.: Tropospheric gravity
709   waves as observed by the high-resolution China radiosonde network and their
710   potential sources, J. Geophys. Res. Atmos., 127, e2022JD037174,

711 https://doi.org/10.1029/2022JD037174, 2022.

712 Zhang, J., J., Guo, S., Zhang, and Shao, J.: Inertia-gravity wave energy and instability

713 drive turbulence: Evidence from a near-global high-resolution radiosonde

714 dataset, Clim. Dyn., 58(11), 2927–2939, https://doi.org/10.1007/s00382-021-

715 06075-2, 2022.

716

717

718

719

720

721

722

723

724

725

726

727

728

729

730

731

732

733

734

735

736

737

738

739

740

741 **Table 1**. Comparisons of mean wind shears between HVRRS and ERA5 reanalysis at

742 heights of 0–2 km a.s.l. (a), 10–15 km a.s.l. (b), and 20–25 km a.s.l. (c).

(a) Wind shear at 0–2 km a.s.l. (m/s/km)

	Polar (NH)	Midlatitude (NH)	Subtropics (NH)	Tropics	Subtropics (SH)	Midlatitude (SH)	Polar (SH)
HVRRS	12.67	12.94	12.30	10.57	13.03	14.16	15.01
ERA5	7.45	7.68	7.78	5.4	8.44	9.67	8.42

(b) Wind shear at 10–15 km a.s.l. (m/s/km)

HVRRS	13.23	14.71	13.02	9.40	13.28	14.64	13.00
ERA5	4.22	6.13	6.82	5.86	6.86	5.20	3.42

(c) Wind shear at 20–25 km a.s.l. (m/s/km)

HVRRS	15.12	15.74	15.41	16.76	16.69	16.12	17.15
ERA5	2.87	3.52	4.06	5.27	3.99	3.36	2.92

743

744

745

746

747

748

749

750

751

752

753

754

755

756

757

758

Table 2. The occurrence rate of low *Ri* at 0.8–1.3 km a.s.l. (a), 2.2–3.2 km a.s.l. (b), 6–15 km a.s.l. (c), and 20–21 km a.s.l. (d). The critical *Ri* (*Rit*) is 1/4 for radiosonde, and it increases from 1/4 to 2 for ERA5 reanalysis. Note that HVRRS data were vertically resampled to 100-m, 200-m, 300-m, and 400-m at these four height intervals to match with the ERA5 reanalysis. In addition, the moving average number in Eq.(1) is 0. RS stands for radiosonde.

(a) Frequency of low *Ri* at 0.8–1.3 km a.s.l. (%) / Vertical resolution of RS is 100-m

	Polar (NH)	Midlatitude (NH)	Subtropics (NH)	Tropics	Subtropics (SH)	Midlatitude (SH)	Polar (SH)
RS, *Rit*=1/4	15.20	24.25	22.86	13.92	22.09	22.43	20.77
ERA5, *Rit*=1/4	2.55	8.88	6.37	2.19	6.80	4.47	2.94
ERA5, *Rit*=0.5	3.77	12.06	9.63	3.65	11.91	7.95	7.22
ERA5, *Rit*=1	8.54	21.22	20.48	8.27	25.45	18.21	15.78
ERA5, *Rit*=1.5	14.18	29.62	30.44	12.88	36.07	27.97	23.22
ERA5, *Rit*=2	19.44	36.58	38.32	17.20	43.72	36.00	29.68

(b) Frequency of low *Ri* at 2.2–3.2 km a.s.l. (%) / Vertical resolution of RS is 200-m

RS, *Rit*=1/4	3.04	6.22	9.00	5.67	9.71	4.29	3.98
ERA5, *Rit*=1/4	0.24	0.60	1.00	1.30	2.26	0.26	0.1
ERA5, *Rit*=0.5	0.37	1.03	1.96	2.10	4.22	0.50	0.18
ERA5, *Rit*=1	1.16	3.26	6.35	5.20	10.00	2.20	0.91
ERA5, *Rit*=1.5	2.77	6.75	12.20	9.00	16.31	5.60	2.68
ERA5, *Rit*=2	5.02	10.85	18.05	13.03	22.45	9.84	5.10

(c) Frequency of low *Ri* at 6–15 km a.s.l. (%) / Vertical resolution of RS is 300-m

RS, *Rit*=1/4	0.76	2.24	3.91	5.98	4.46	1.98	0.59
ERA5, *Rit*=1/4	0.10	0.38	0.54	1.46	0.56	0.24	0.05
ERA5, *Rit*=0.5	0.32	1.16	1.95	4.36	2.10	0.93	0.15
ERA5, *Rit*=1	1.37	4.33	7.72	13.14	8.89	3.51	0.61
ERA5, *Rit*=1.5	2.93	8.31	14.54	21.78	17.05	6.76	1.38
ERA5, *Rit*=2	4.70	12.35	20.91	29.28	24.55	10.02	2.32

(d) Frequency of low Ri at 20–21 km a.s.l. (%) / Vertical resolution of RS is 400-m						
RS, Rit=1/4	0.03	0.07	0.13	0.04	0.04	0.10	0.07
ERA5, Rit=1/4	0.01	0.02	0.01	0.02	0.02	0.03	0.04
ERA5, Rit=0.5	0.02	0.03	0.01	0.02	0.03	0.04	0.04
ERA5, Rit=1	0.03	0.05	0.04	0.05	0.05	0.08	0.04
ERA5, Rit=1.5	0.04	0.11	0.13	0.19	0.09	0.17	0.04
ERA5, Rit=2	0.05	0.21	0.32	0.55	0.18	0.30	0.05

765

766

767

768

769

770

771

772

773

774

775

776

777

778

779

780

781

782

783

784

785

786

787 **Table 3**. Vertical wind shears at 0.8–1.3 km a.s.l. (a), 2.2–3.2 km a.s.l. (b), 6–15 km

788 a.s.l. (c), and 20–21 km a.s.l. (d). Note that HVRRS data was vertically resampled to

789 100-m, 200-m, 300-m, and 400-m at these four height intervals to match with the ERA5

790 reanalysis. RS stands for radiosonde.

(a) Wind shear at 0.8–1.3 km a.s.l. (m/s/km) / Vertical resolution of RS is 100-m						
	Polar (NH)	Midlatitude (NH)	Subtropics (NH)	Tropics	Subtropics (SH)	Midlatitude (SH)	Polar (SH)
RS	12.50	13.63	11.80	9.83	13.54	13.06	13.85
ERA5	5.43	5.92	6.47	4.83	7.02	6.71	6.05
(b) Wind shear at 2.2–3.2 km a.s.l. (m/s/km)/ Vertical resolution of RS is 200-m						
RS	8.31	9.09	9.24	9.08	9.45	9.39	10.00
ERA5	3.72	4.47	5.19	4.65	5.41	4.71	4.19
(c) Wind shear at 6–15 km a.s.l. (m/s/km) / Vertical resolution of RS is 300-m						
RS	8.30	9.50	9.41	7.72	9.80	9.38	8.00
ERA5	4.00	5.22	5.84	5.21	6.14	4.76	3.37
(d) Wind shear at 20–21 km a.s.l. (m/s/km) / Vertical resolution of RS is 400-m						
RS	9.02	10.40	11.67	12.56	12.14	10.48	9.80
ERA5	3.00	3.83	4.79	5.59	4.72	3.63	2.98

791

792

793

794

795

796

797

798

799

800

801

802 **Table 4**. Similar to Tab.1 but for the occurrence frequency of $Ri<Rit$. Note that Rit is

803 indicated by $Ri<1/4$ in radiosonde, but it is identified with 1 in ERA5 reanalysis.

(a) $OF(Ri<Rit)$ at 0–2 km a.s.l. (%)

	Polar (NH)	Midlatitude (NH)	Subtropics (NH)	Tropics	Subtropics (SH)	Midlatitude (SH)	Polar (SH)
HVRRS	9.56	16.10	15.78	13.08	16.98	15.38	13.97
ERA5	26.91	33.85	35.70	37.27	40.56	40.46	26.55

(b) $OF(Ri<Rit)$ at 10–15 km a.s.l. (%)

HVRRS	0.53	2.22	5.44	11.22	6.17	1.55	0.62
ERA5	0.44	2.62	6.86	17.03	7.15	1.67	0.28

(c) $OF(Ri<Rit)$ at 20–25 km a.s.l. (%)

HVRRS	0.36	0.49	0.43	0.5	0.40	0.67	1.35
ERA5	0.06	0.07	0.04	0.1	0.06	0.06	0.04

804

805

806

807

808

809

810

811

812

813

814

815

816

817

818

819
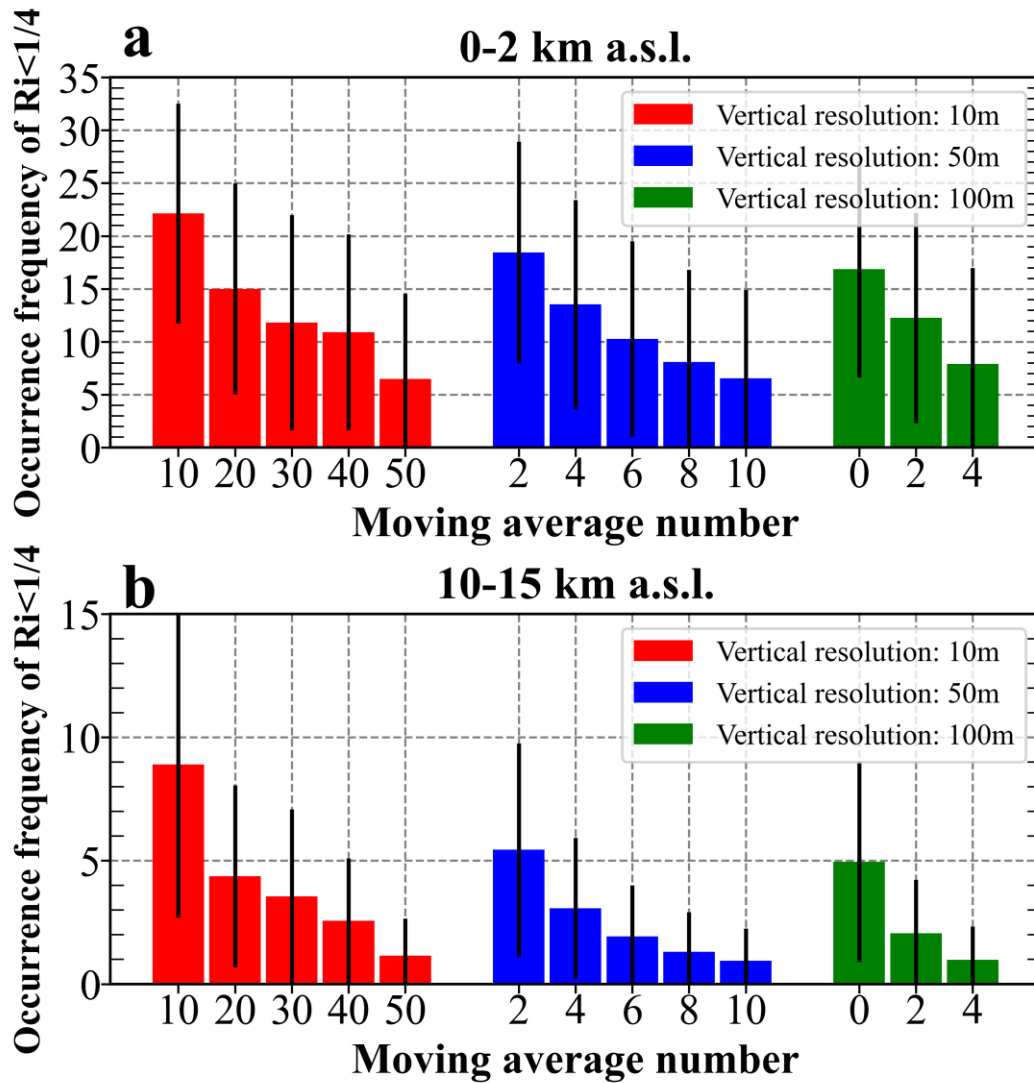
Figure 1. The averaged occurrence frequencies of $Ri<1/4$ at heights of 0–2 km a.s.l. (a) and 10–15 km a.s.l. (b), with vertical resolutions ranging 10-m to 100-m and moving point numbers increasing from 0 to 50. The error bars correspond to the standard deviation. The metrics are counted based on all radiosonde profiles during years 2017–2022.
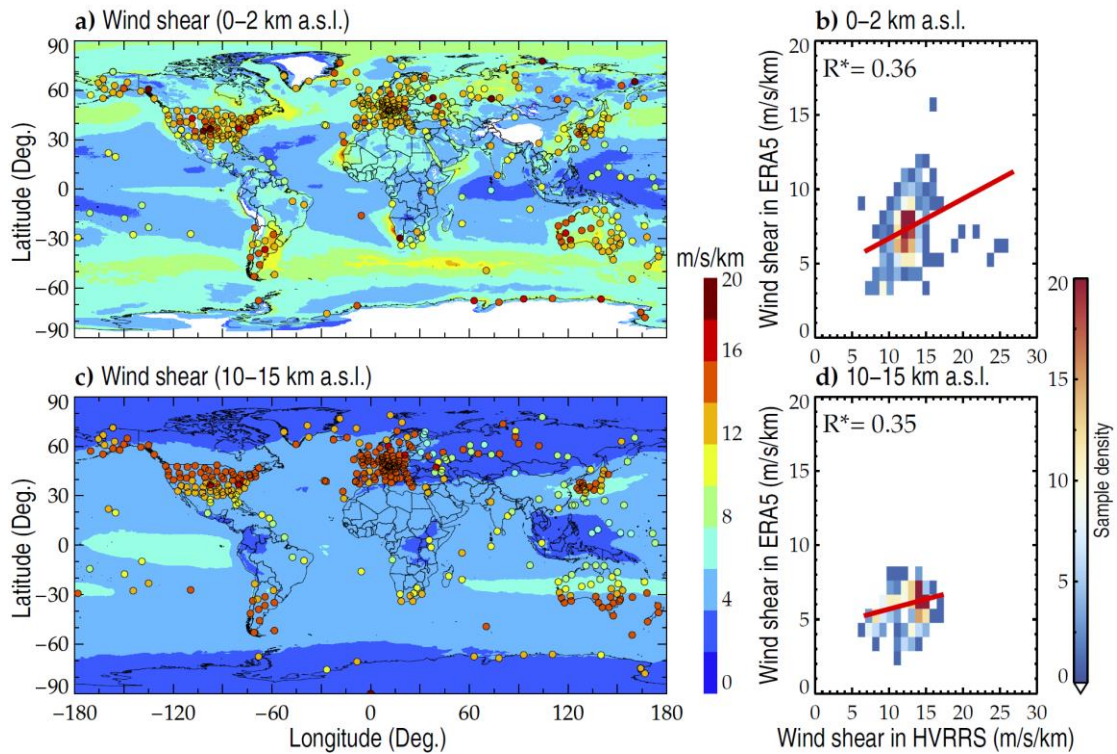
Figure 2. The spatial distribution of mean wind shear in ERA5 reanalysis at heights of 0–2 km a.s.l. (a) and 10–15 km a.s.l. (c), where the areas with a near-surface pressure lower than 800 hPa are masked with white. The overlaid colored circles represent the result in HVRRS at the same height levels. Each data point represents a vertically averaged value of the wind shear at one radiosonde station during the whole study period. Density plots (b, d) show the correlation between wind shears in HVRRS and ERA5 reanalysis. The ERA5 derived wind shears are spatially and temporally collocated with those of HVRRS. In addition, the red lines represent a least-squared linear regression, and the star superscripts indicate that values are statistically significant ($p<0.05$).
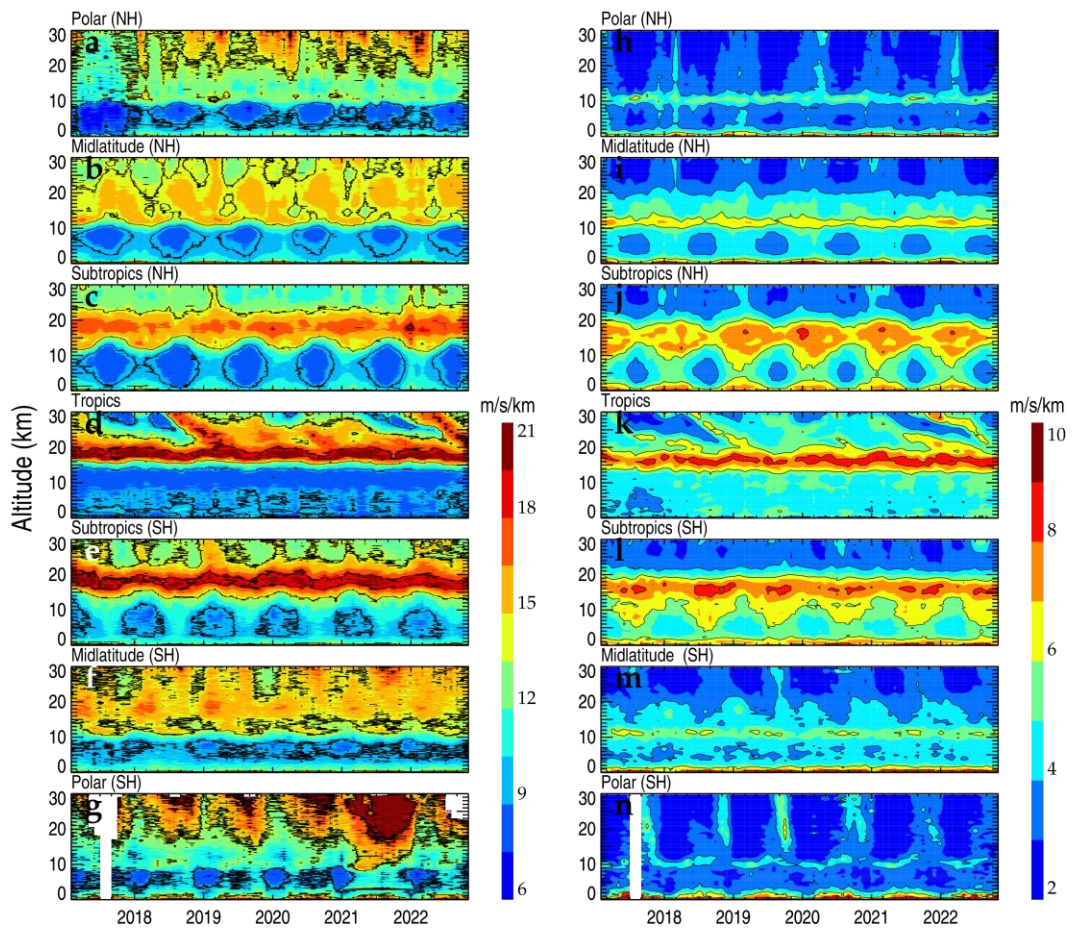
Figure 3. Monthly mean wind shears during years 2017–2022 in HVRRS (a–g) and ERA5 reanalysis (h–n) at different climate zones. The ERA5 derived wind shears are spatially and temporally collocated with those of HVRRS. NH=Northern Hemisphere; SH=Southern Hemisphere.
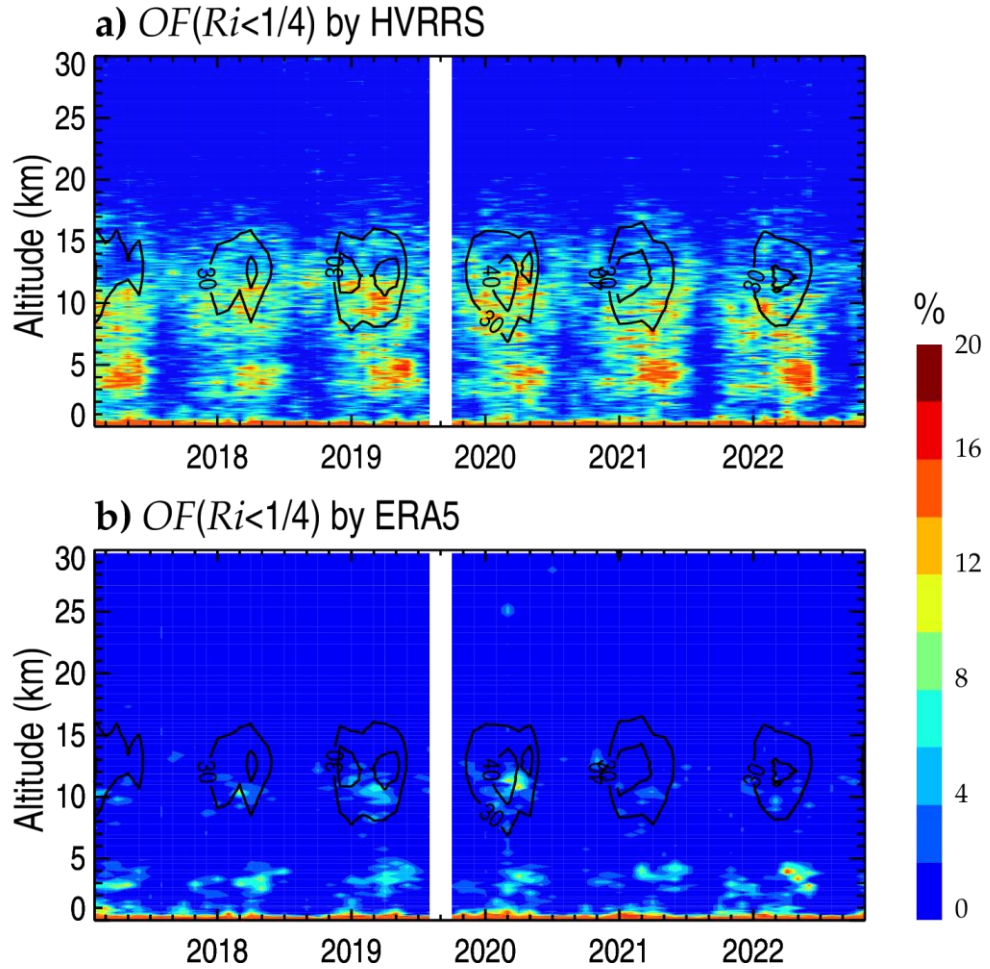
Figure 4. The monthly occurrence frequency of $Ri<1/4$ at Corpus Christi station (27.77° N, −97.5° W) in HVRRS (a) and ERA5 reanalysis (b). Note that the contour curves in (a) and (b) concern the mean horizontal wind speed, and that the ERA5 derived quantities are spatially and temporally collocated with those of HVRRS.
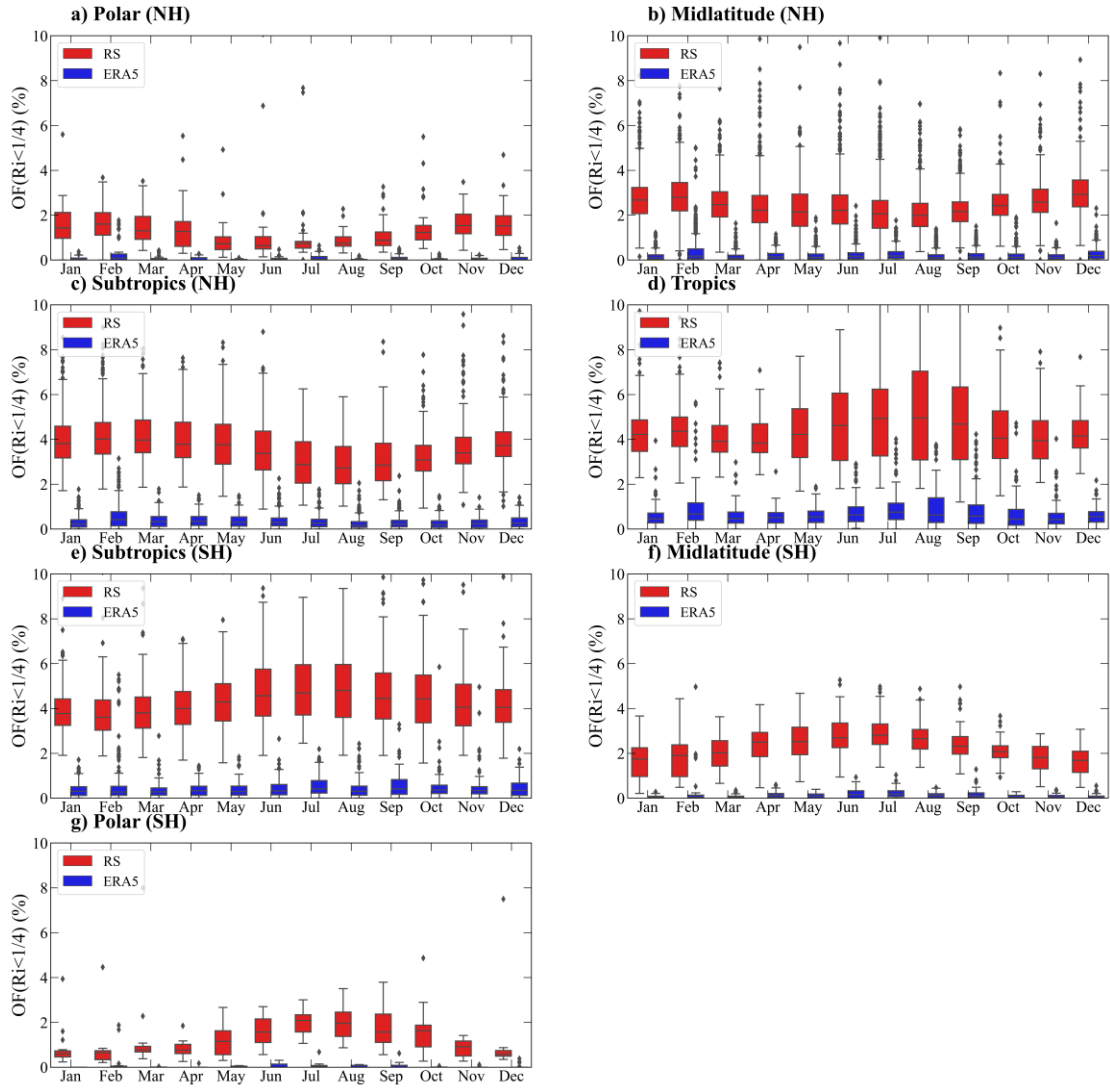
Figure 5. The annual cycles of the occurrence frequency of $Ri<1/4$ in different climate zones at 10–15 km a.s.l.. The red and blue boxes represent the frequencies in HVRRS and ERA5 reanalysis, respectively. The ERA5 derived Ri is spatially and temporally collocated with that of HVRRS. NH, Northern Hemisphere; SH, Southern Hemisphere.
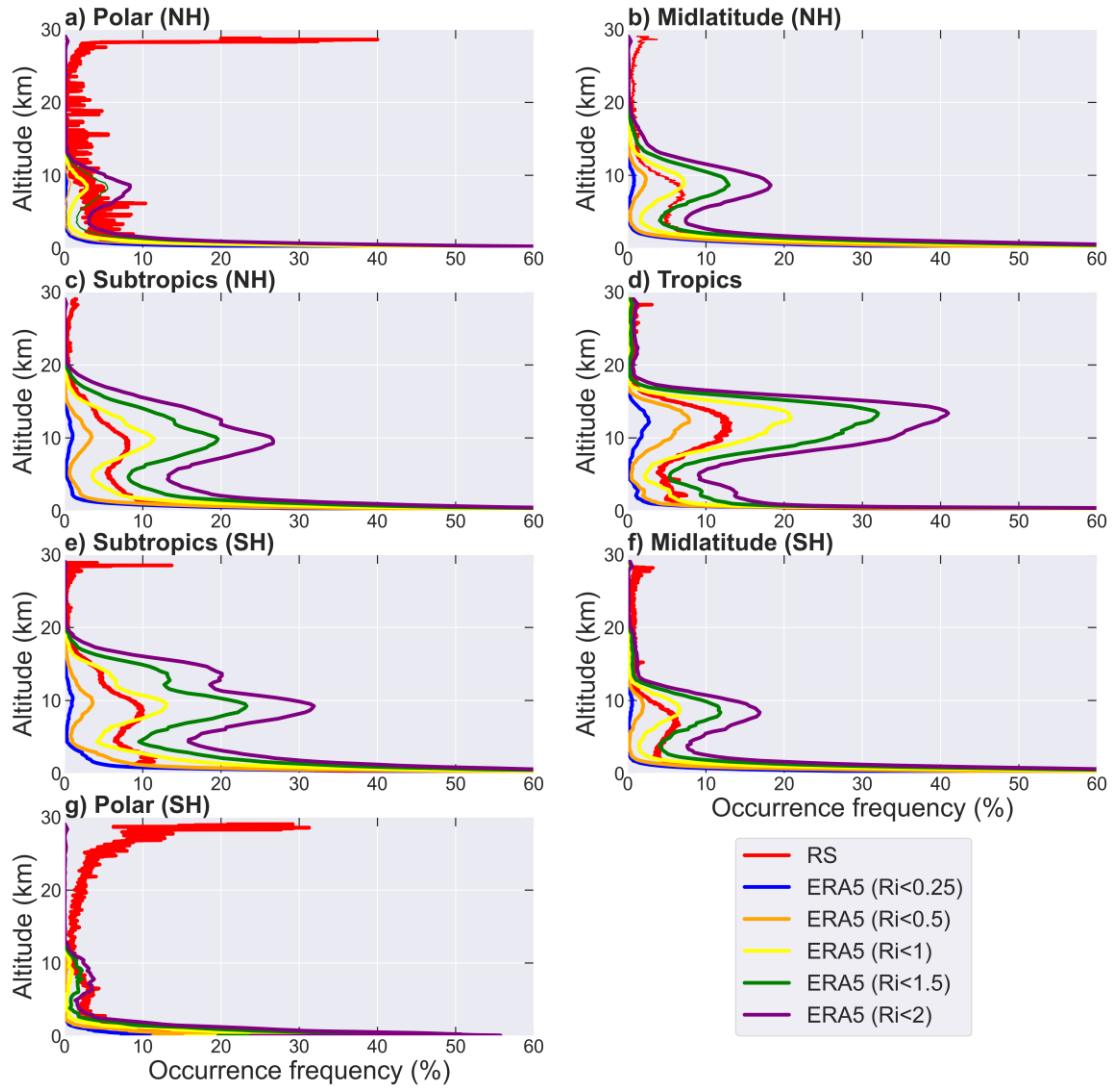
Figure 6. The altitude variation of the occurrence frequency of *Ri* below certain thresholds (0.25, 0.5, 1, 1.5, and 2) in ERA5 reanalysis in various climate zones. The ERA5 derived *Ri* is spatially and temporally collocated with that of HVRRS. The occurrences of *Ri*<1/4 in HVRRS are overlapped with red lines.
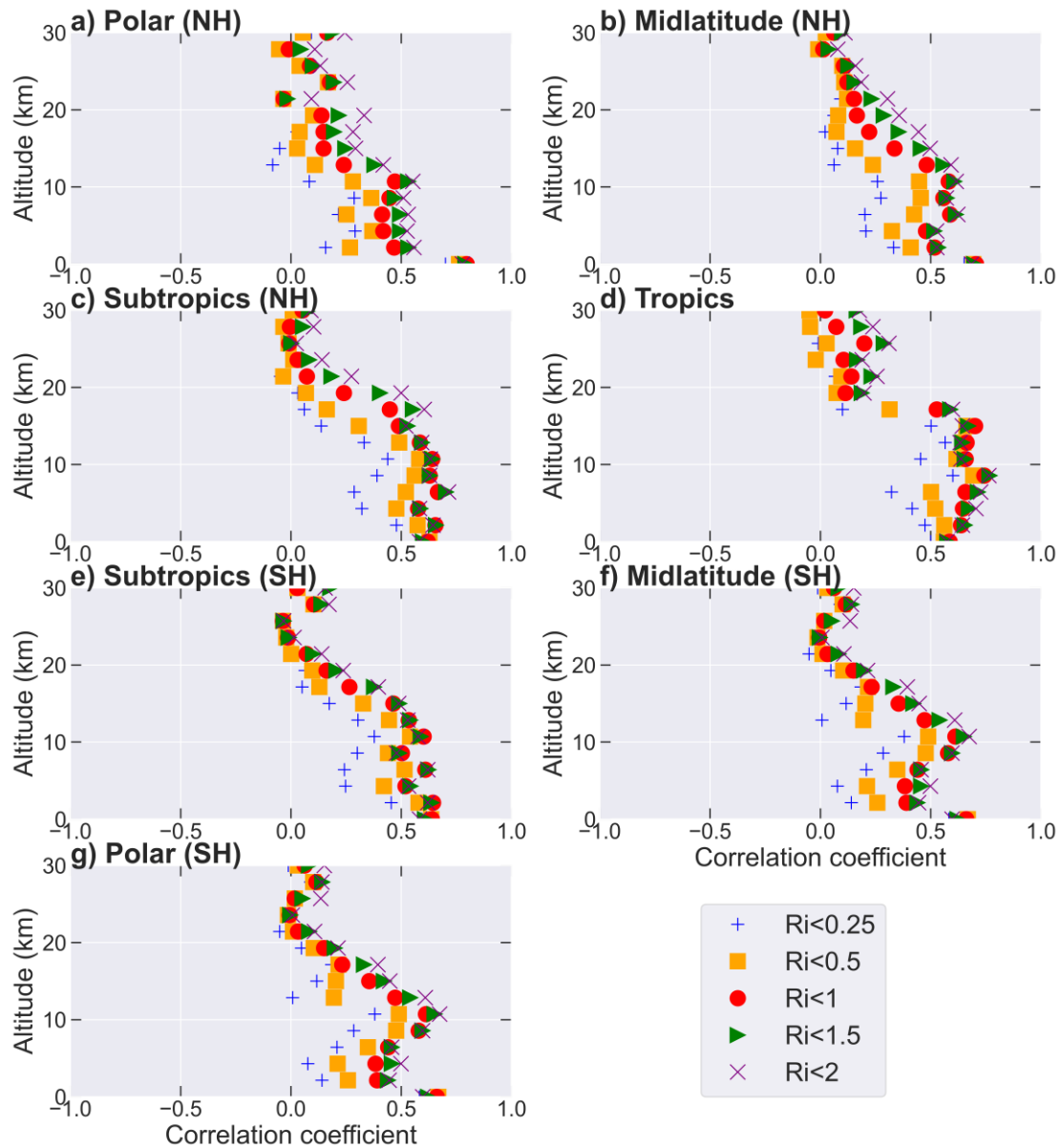
Figure 7. The correlation coefficients between monthly averaged occurrence frequency of $Ri<1/4$ in the HVRRS and the monthly occurrence frequency of Ri below certain thresholds (0.25, 0.5, 1, 1.5, and 2) in ERA5 reanalysis. The ERA5 derived Ri is spatially and temporally collocated with that of HVRRS. The coefficients in various climate zones are estimated in an increment of 2 km.
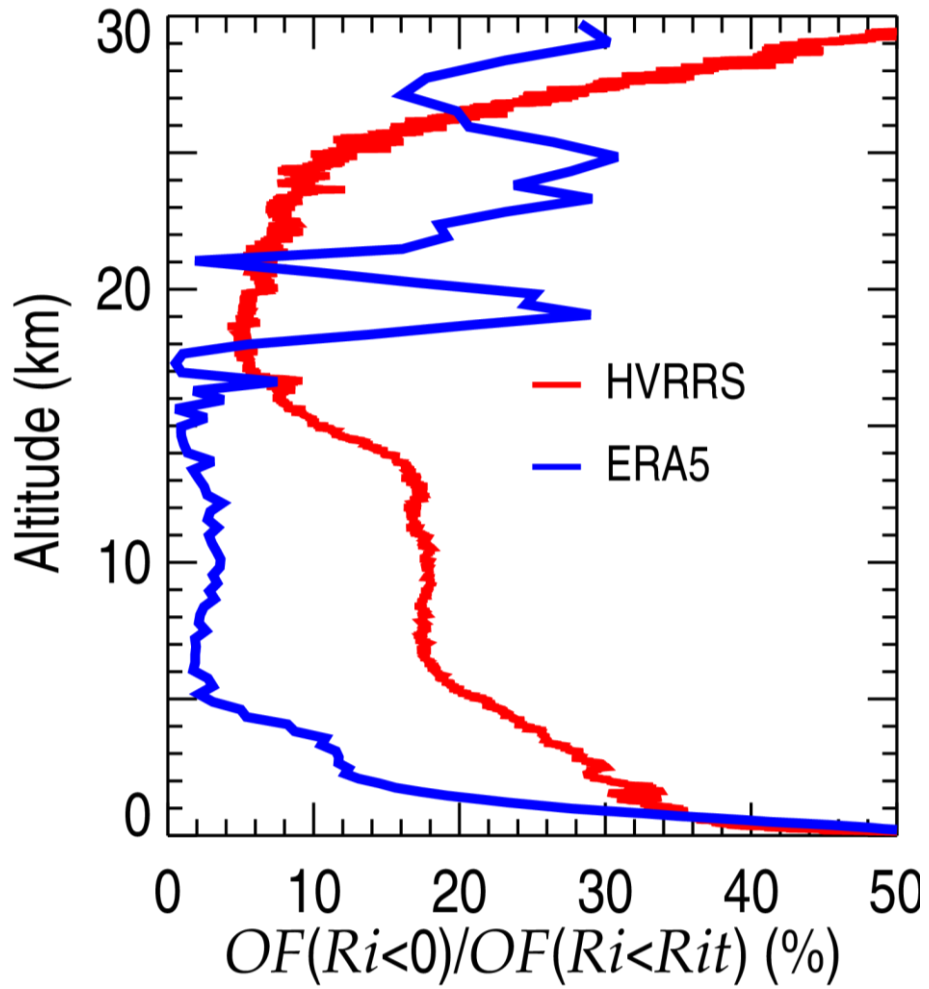
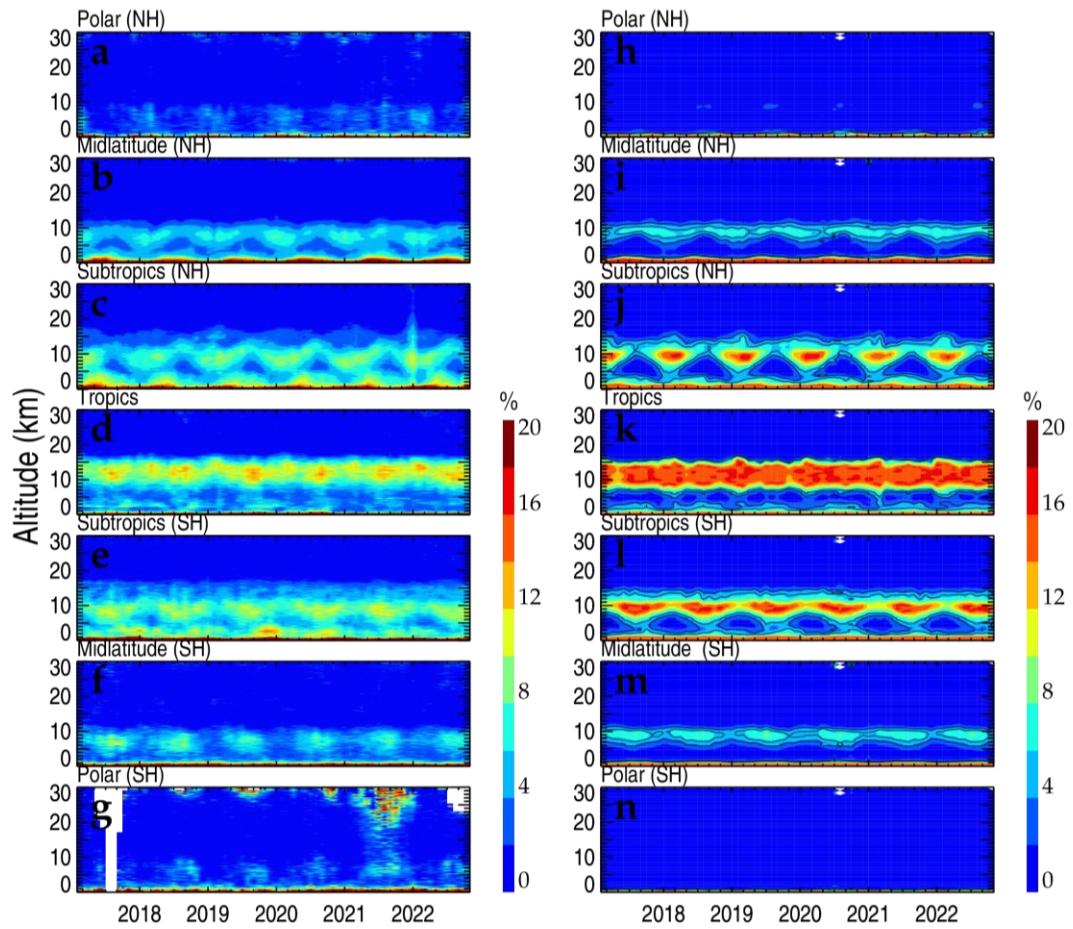**Figure 8**. The percentage of *OF(Ri<0)* relative to *OF(Ri<Rit)* in HVRRS (red) and ERA5 reanalysis (blue).

a) *OF(Ri<Rit)* at 0–2 km a.s.l.
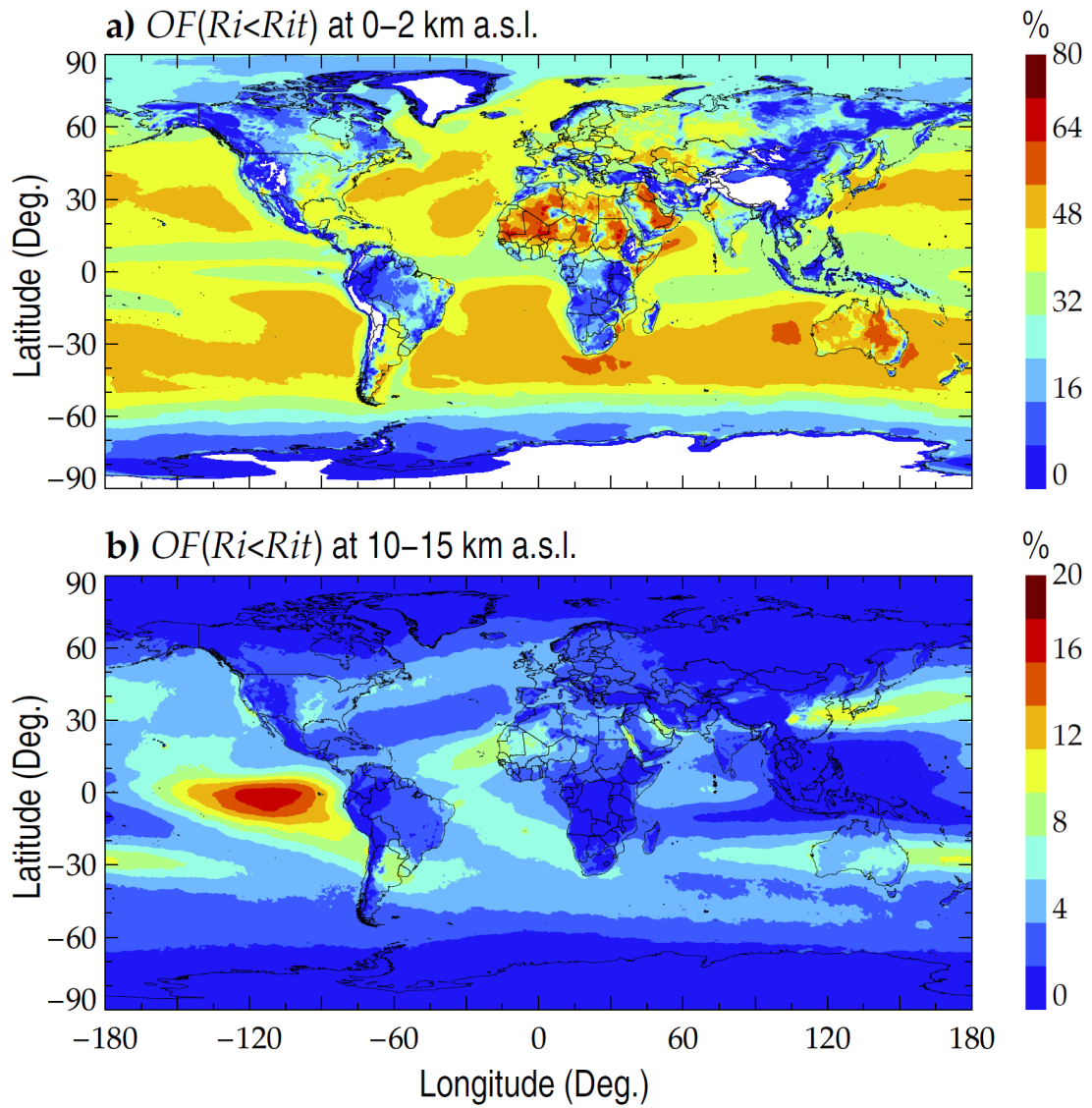
b) *OF(Ri<Rit)* at 10–15 km a.s.l.

Figure 9. The spatial distribution of the mean *OF(Ri<Rit)* in ERA5 reanalysis at 0–2 km a.s.l. (a) and 10–15 km a.s.l. (b). Note that *Rit* is set to 1.
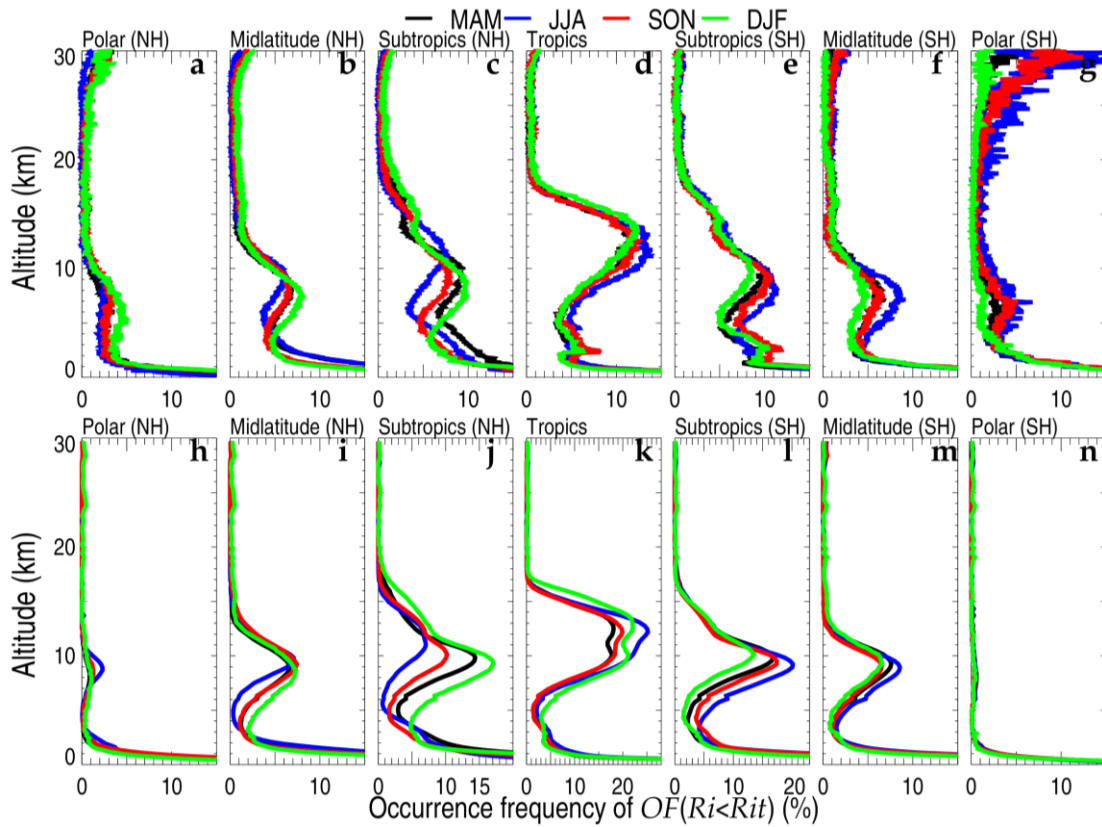
**Figure 10**. The monthly averaged *OF*(*Ri*<*Rit*) in the HVRRS (a–g) and ERA5 reanalysis (h–n) in seven climate zones. NH=Northern Hemisphere; SH=Southern Hemisphere.

Figure 11. The seasonal averaged $OF(Ri<Rit)$ in the HVRRS (a–g) and ERA5 reanalysis (h–m) in seven climate zones. MAM, March–April–May; JJA, June–July–August; SON, September–October–November; DJF, December–January–February. NH=Northern Hemisphere; SH=Southern Hemisphere.
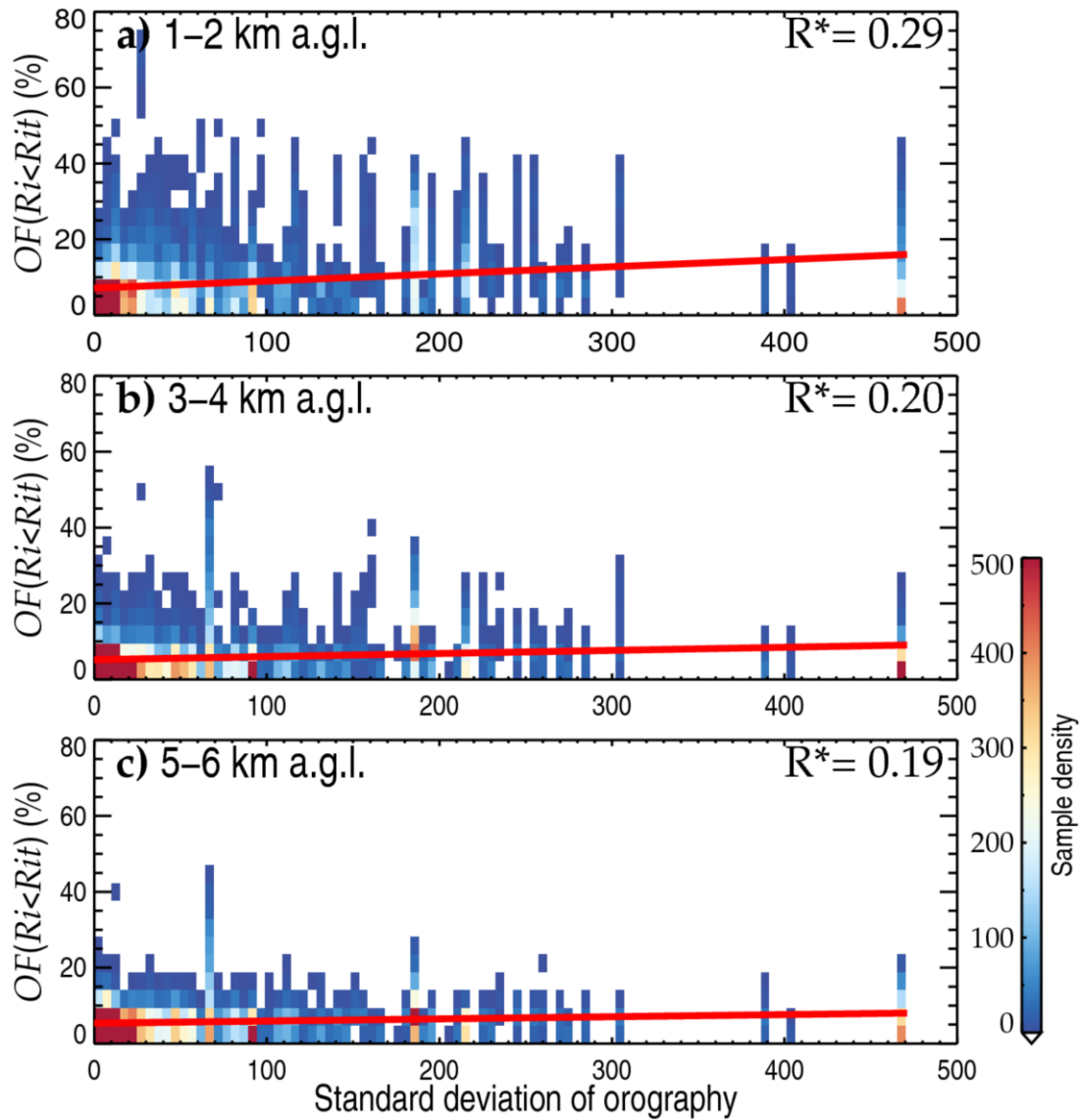
Figure 12. The association of HVRRS-determined $OF(Ri<Rit)$ with different standard deviations of orography (dimensionless). (a), (b), and (c) are for height ranges of 1–2 km, 3–4 km, and 5–6 km a.g.l., respectively. The correlation coefficients between $OF(Ri<Rit)$ and standard derivation of orography are marked in the top right corner, where the star superscripts indicate that values are statistically significant ($p<0.05$).

887

888
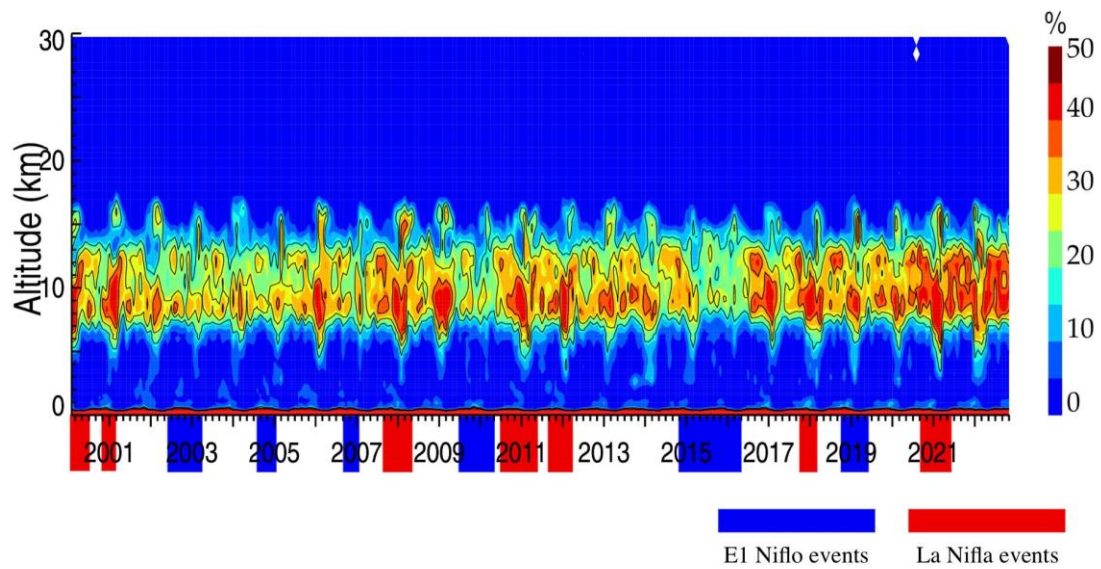
Figure 13. The monthly averaged *OF*(*Ri<Rit*) in ERA5 reanalysis over the Niño 3 region (5° N–5° S, 150° W–90° W). The blue and red shadings in time axis indicate the time periods with EI Niño and La Niña events, respectively.
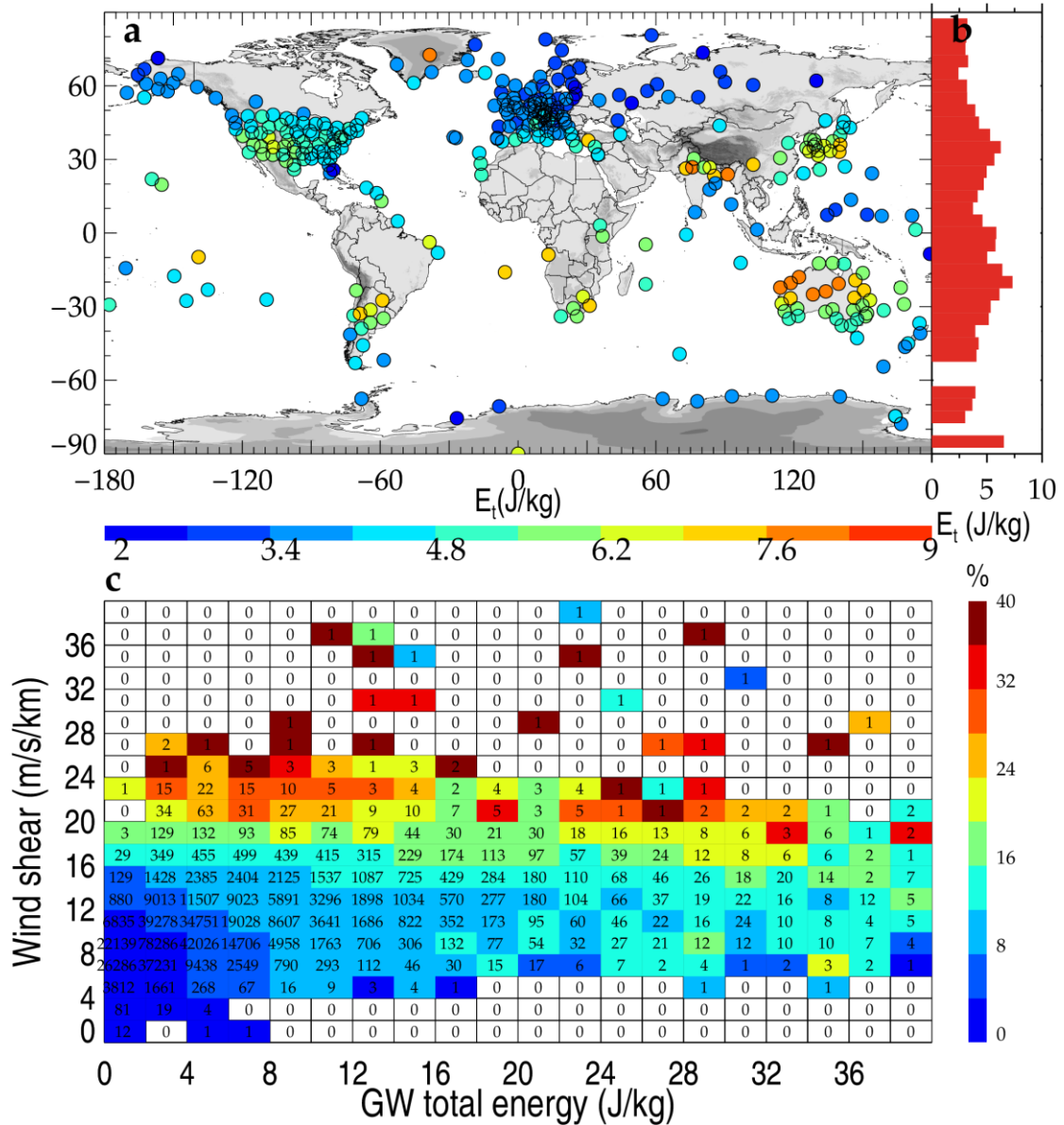
Figure 14. Geographical distribution of mean tropospheric GW total energy obtained from the HVRRS (a). The latitudinal variation of mean energy in a grid cell of 5° latitude (b). The joint distribution of *OF*(*Ri*<*Rit*) with GW energy and wind shear (c). The *OF*(*Ri*<*Rit*) and wind shear are derived from individual HVRRS profiles and vertically averaged over the tropospheric segment that is used for GW study. The numerical number in (c) indicates the matched profile number in each grid, using a bin size of 2 J/kg along the x axis and 2 m/s/km along the y axis.

Figure 15. Joint distribution of HVRRS-derived wind speed, wind shear, and *OF*(*Ri<Rit*), with a bin size of 5 m/s along the x axis and 5 m/s/km along the y axis. Note that all the relationship is based on the mean result of individual profiles at heights of 10–15 km a.s.l.. The number indicates the matched profile number in each grid.